

A simple estimation of equatorial Pacific response from windstress to untangle Indian Ocean Dipole and Basin influences on El Niño

T. Izumo¹, J. Vialard¹, H. Dayan¹, M. Lengaigne^{1,2}, I. Suresh³

¹ LOCEAN, IPSL, Sorbonne Universités (UPMC, Univ Paris 06)-CNRS-IRD-MNHN, Paris, France

² Indo-French Cell for Water Sciences, IISc-NIO-IITM-IRD Joint International Laboratory, NIO, Dona Paula, India

³ CSIR-National Institute of Oceanography (NIO), Goa, India

Corresponding author: Takeshi Izumo

LOCEAN - Case 100; Case 100 - Université P. et M. Curie; 4, Place Jussieu – 75252

Paris Cedex 05; FRANCE

E-mail: takeshi.izumo@locean-ipsl.upmc.fr

Abstract

Sea Surface Temperature (SST) anomalies that develop in spring in the central Pacific are crucial to the El Niño Southern Oscillation (ENSO) development. Here we use a linear ocean model, and its impulse response to a typical ENSO wind pattern, to derive a simple equation that relates those SST anomalies to the low frequency evolution of zonal wind stress anomalies τ_x over the preceding months. We show that SST anomalies can be approximated as a “causal” filter of τ_x , $\tau_x(t-t_1) - c\tau_x(t-t_2)$, where t_1 is $\sim 1-2$ months, t_2-t_1 is ~ 6 months and c ranges between 0 and 1 depending on τ_x location (i.e. SST anomalies are approximately proportional to the wind stress anomalies 1-2 months earlier minus a fraction of the wind stress anomalies 7-8 months earlier). The first term represents the fast oceanic response, while the second one represents the delayed negative feedback associated with wave reflection at both boundaries.

This simple approach is then applied to assess the relative influence of the Indian Ocean Dipole (IOD) and of the Indian Ocean Basin-wide warming/cooling (IOB) in favouring the phase transition of ENSO. In agreement with previous studies, Atmospheric General Circulation Model experiments indicate that the equatorial Pacific wind responses to the IOD eastern and (IOB-related) western poles tend to cancel out during autumn. The abrupt demise of the IOD eastern pole thus favours an abrupt development of the IOB-cooling-forced westerly wind anomalies in the western Pacific in winter-spring (*vice versa* for an IOB warming). As expected from the simple SST equation above, the faster wind change fostered by the IOD enhances the central Pacific SST response as compared to the sole IOB influence. The IOD thereby enhances the IOB tendency to favour ENSO phase transition. As the IOD is more independent of ENSO than the IOB, this external influence could contribute to enhanced ENSO predictability.

Keywords: El Niño Southern Oscillation (ENSO); equatorial Pacific ocean dynamics; atmospheric teleconnections; Indian Ocean Dipole mode (IOD) and Basin-wide warming/cooling (IOB); convolution to impulse response of a linear system

1) Introduction

The El Niño Southern Oscillation (ENSO) is the main mode of interannual climate variability, with huge environmental and socio-economic impacts (e.g. McPhaden et al. 2006). ENSO-induced changes in deep atmospheric convection in the central Pacific have worldwide climatic impacts through atmospheric teleconnections (e.g. Trenberth et al. 1998). Despite the importance of accurate forecasts, ENSO is still difficult to predict at long leads (e.g. Barnston et al. 2011, Clarke 2014).

The mechanisms leading to El Niño growth and termination are now reasonably well understood. The development of an El Niño event in boreal spring and summer results from the Bjerknes positive feedback. In this feedback, a positive Sea Surface Temperature anomaly (hereafter SSTA) enhances deep atmospheric convection in the central Pacific, resulting in westerly wind anomalies (Gill, 1980) and eastward surface currents that advect the warm pool eastward, thereby reinforcing the initial SSTA (e.g. Picaut et al. 1996, Vialard et al; 2001). This positive feedback mechanism is offset by several negative feedbacks: the instantaneous negative feedback from air to sea fluxes (e.g., Lloyd et al. 2010), and the delayed feedbacks resulting from oceanic dynamics (and in particular oceanic wave reflections, e.g. Boulanger and Menkes 2001, Boulanger et al. 2004) and from non-linear interactions of convective anomalies with the seasonal cycle (e.g., Lengaigne et al. 2006). Those negative feedbacks eventually terminate El Niño events during the following winter.

It is however still difficult to accurately predict the onset of an El Niño event. An anomalously positive “Warm Water Volume” (WWV, the total volume of water above 20°C equatorward of 5° in the Pacific ocean), referred to as a “recharged state”, acts as a favourable condition for an El Niño to develop (e.g. Meinen and McPhaden 2000). The WWV index thus provides predictability of 6 to 9 months before El Niño peaks. It is however difficult to predict ENSO at longer lead times due to the so-called spring predictability barrier (Barnston et al. 2011), partly because of the influence of stochastic intraseasonal variability (e.g. Lengaigne et al. 2004). Several studies have however identified ENSO precursors at longer leads in various regions outside of the tropical Pacific, particularly in the Indian Ocean (e.g. Meehl et al. 2003), and exploited those predictors to obtain an increased predictability at long leads (e.g., Clarke and Van Gorder 2003, Izumo et al. 2010, 2014). Accordingly, including the Indian Ocean in climate models tends to improve their ENSO forecasting skills (e.g. Yamanaka et al. 2009, Luo et al. 2010, Ohba and Watanabe 2012).

There are two main patterns of interannual SST variability in the tropical Indian Ocean. The Indian Ocean Basin-wide warming/cooling (hereafter IOB) is essentially the Indian Ocean response to ENSO (e.g. Schott et al. 2009, for a review; their Fig. 12). During an El Niño event, the entire tropical Indian Ocean indeed warms in response to reduced nebulosity and surface wind speed resulting from anomalous subsidence associated with zonal shifts in the Walker circulation (Klein et al. 1999; Shinoda et al. 2004b; Ohba and Ueda 2005, 2009b; Xie et al. 2009). This warming lasts for two seasons after the peak of ENSO, possibly maintained by local air-sea interactions over the Indian Ocean (Xie et al. 2009, Du et al. 2009, Izumo et al. 2008). Several modelling studies showed that this IOB warming produces an easterly wind anomaly over the western Pacific in winter (e.g., Annamalai et al. 2005), which favours the phase transition to La Niña (e.g., Kug and Kang 2006; Ohba and Ueda 2007). Jansen et al. (2009) and Frauen and Dommenges (2012) suggested that the IOB indeed influences the ENSO cycle, but without much benefit for ENSO predictability, possibly because of its strong association to ENSO itself (Izumo et al. 2014).

The Indian Ocean is also home to intrinsic SST interannual variability. A positive Indian Ocean Dipole (pIOD) is characterized by negative SSTA in the eastern Indian Ocean near the coast of Sumatra and weaker positive SSTA in the western Indian Ocean (*vice versa* for negative IOD; hereafter nIOD). As for ENSO, the Bjerknes feedback allows the IOD to grow during boreal summer and peak in fall (e.g. Reverdin et al. 1986; Saji et al. 1999; Webster et al. 1999; Murtugudde et al. 2000), with surface fluxes also playing an important role in its seasonal amplification and termination (Hendon 2003, Shinoda et al. 2004b). IOD events can occur independently of ENSO, despite a tendency for El Niños (La Niñas) to trigger pIODs (nIODs), with ~40% of variance in common (Fig. 1d). Several studies suggest that the IOD eastern pole is the most relevant one in terms of dynamics (e.g. Shinoda et al. 2004a) and that the western pole SST signal is mostly associated with the remote forcing from ENSO when both phenomena co-occur (e.g. Zhao and Nigam 2015). Statistical analyses by Izumo et al. (2010, 2014) show that nIODs (pIODs) tend to be followed by El Niño (La Niña) events 14 months later. They further demonstrated a significant skill in predicting ENSO peak amplitude 14 months in advance by jointly using IOD and WWV as predictors in a simple linear regression model. They suggested the following mechanism: the warm eastern pole of a nIOD induces an easterly anomaly in the equatorial Pacific, that abruptly disappears at the termination of the IOD event (in November-December, see e.g. Shinoda et al. (2004a) for a detailed description of the IOD eastern pole termination processes). The oceanic response to this abrupt wind change induces

a positive SSTA in the central Pacific in spring, further amplified by the Bjerknes feedback to possibly culminate into an El Niño at the end of the following year. This IOD influence on following year's ENSO state is significant in most CMIP5 models (Jourdain et al. 2015). The question of the respective influences of the IOB and IOD on ENSO evolution and predictability remains open, with Izumo et al. (2014), Dayan et al. (2014a) and Jourdain et al. (2015) all suggesting that the IOD brings more ENSO predictability than the IOB.

Dayan et al. (2014b) investigated the western equatorial Pacific wind response to the combined influence of an IOD and an IOB, through sensitivity experiments with an AGCM. Their results suggest that a statistically significant wind response only occurs in late boreal winter after the IOD demise. Fig. 1a,b,c shows the atmospheric response of the AGCM used in Dayan et al. (2014b) during a nIOD in September-November and during the IOB cooling that follows in January-March. During winter and spring, the IOB cooling is fully developed and decreases rainfall / convective heating over the Indian Ocean (see e.g. Dayan et al. 2014b, their Fig. 11). This Indian Ocean tropospheric forcing induces an atmospheric Kelvin wave (see e.g. Watanabe and Jin 2002, Annamalai et al. 2005, Ohba and Ueda 2007, Annamalai et al. 2010) which drives westerly anomalies in the western Pacific from around January to March (Fig. 1c). On the other hand, there is no clear wind anomaly in the western Pacific during the nIOD peak in autumn (Fig. 1a,c), presumably because the response to the nIOD warm eastern pole (Fig. 1a) induces a rainfall increase and hence an atmospheric Kelvin wave response that tends to cancel out the Kelvin wave response induced by the SST and rainfall negative anomalies in the rest of the basin (Annamalai et al. 2005, 2010), the two poles being zonally relatively close (Gill 1980). The results of Dayan et al. (2014b) confirm the role of the ENSO-induced IOB in the phase transition of ENSO but *apparently* contradict the mechanisms proposed by Izumo et al. (2010) to explain the influence of nIODs (resp. pIOD) on following year's El Niño (resp. La Niña).

Izumo et al. (2010) have indeed emphasized the role of western Pacific easterly wind anomalies in autumn, resulting from the nIOD warm eastern pole forcing. On the other hand, Dayan et al. (2014b) and e.g. Annamalai et al. (2005, 2010) have rather focussed on the IOB-driven westerly anomalies that follow in late winter/spring, because the effects of the IOD eastern and western poles would tend to compensate earlier. But then, how can we explain the IOD influence on following year's ENSO suggested by Izumo et al. (2010, 2014)?

In the current paper, we will investigate the following hypothesis to explain the IOD influence on following year's ENSO. The western Pacific wind response to the succession of a nIOD (Fig.

1a) and IOB cooling (Fig. 1b) depicted on Fig. 1c is associated with an abrupt development of the westerly wind anomaly in December-January. Our hypothesis is that this abrupt development is due to the occurrence of the nIOD before the IOB cooling, i.e., there is a compensation between the atmospheric responses to the western pole (partly an IOB signature) and eastern pole of the IOD that prevents a wind response on the western Pacific (Annamalai et al. 2005, 2010) until the disappearance of the IOD in late November. The quick disappearance of the eastern pole of the IOD in November then allows the response to the now basin-wide cold anomalies to induce quickly-developing westerly wind anomalies in the western Pacific afterward. Physically, in the fast-wave limit (i.e. slow changes of the wind compared with the basin adjustment time), the thermocline zonal gradient tends to balance zonal wind stress (hereafter τ_x). Wind variations at shorter timescales induce a larger imbalance between the wind stress and pressure gradient, and hence a stronger oceanic response. Our working hypothesis is thus that the IOD could favour *a delayed but faster appearance* of IOB-forced zonal wind anomalies in the western Pacific, and hence a stronger equatorial wave oceanic adjustment and resulting SST anomaly in the central Pacific, favouring ENSO phase reversal.

In the current paper, we will use the linear, continuously-stratified, ocean model (LCS) of McCreary (1980), combined with a simple linear SST equation, to explore the differences in oceanic response to wind anomalies that appear either progressively (i.e., a “pure” IOB) or abruptly (an IOB preceded by an IOD) in the western Pacific. This relatively simple but rather realistic ocean model is introduced in Section 2. In section 3, we demonstrate that the ocean responds more to “quick” than to “slow” wind variations by deriving a simple formula between zonal windstress forcing in the western or central Pacific and the SST response in the central Pacific. This formula is then applied in section 4 to compare the oceanic responses to various idealised wind forcings mimicking IOD or IOB influences. Experiments using a more realistic wind forcing are then discussed in section 5. Section 6 summarizes and discusses the interests and limits of the present study.

2) Data, model and validation

2.1) Observational datasets and indices

In the present paper, we use a variety of observational datasets. We use *in situ* near-surface current (U) and depth of the 20°C isotherm z_{20} (a proxy of thermocline depth H), derived from the TAO/TRITON mooring array (McPhaden et al. 1998, <http://www.pmel.noaa.gov/tao>) to

validate our simple ocean model. Data with quality control flags 4 and 5 are discarded. We estimate surface current as the 0-20 m average, using current meters in priority and ADCP (Acoustic Doppler Current profiler) when current meters are not available. We also use complementary satellite products for the model validation, because of *in situ* observational uncertainties and gaps: AVISO multi-satellite sea surface height (SSH) as well as OSCAR (Lagerloef et al. 1999) current estimates at 15m depth. We use two satellite-based SST datasets: OISSTv2 (Reynolds et al. 2002) is used for the model validation and interpolated TMI (Wentz et al. 2000) SST, which is more accurate but available over a much shorter period, is used in the simple SST equation of the ocean model to estimate the climatological SST gradient. Wind stresses from ERA-Interim (ERA-I) atmospheric reanalysis (Dee et al. 2011) are used to force the control run of our linear ocean model and ERA-I SST (which is a blend of various observational SST products) is used to compute the various forcing for the AGCM. We also use the historical observational HadISST (Rayner et al. 2003) SST product over 1871-2008, to test the robustness of some results over a longer period.

As for indices, we will use the Niño3.4 SST index, a commonly used index for ENSO variability, that corresponds to averaged SSTA in the central-eastern equatorial Pacific (5°S–5°N; 170°W–120°W). While SSTA there are a good measure of ENSO mature phase, the atmosphere is more sensitive to SSTAs in the central Pacific. We will hence also use a central equatorial Pacific SST index: « Niño4_{eq} », which is equivalent to the Niño4 index, but focussed on the equatorial waveguide, (160°E-150°W, 2°N-2°S against 5°N-5°S for Niño4). Using Niño4 instead of Niño4_{eq} gives qualitatively similar results, but reduces the SST variability by a factor of ~2. We use the typical Dipole Mode Index (DMI; Saji et al. 1999) to characterize the IOD. IOB is characterized using an index defined as the 40°E-110°E, 20°N-20°S averaged SSTA over January-March as in Izumo et al. (2014).

Interannual monthly anomalies are calculated by removing the mean seasonal cycle (for all figures) and by further applying a 5 points Hanning filter to emphasize periods of 3 months or more for the validations (for Figs 2 and 4, and Table 1). For statistical analyses on the 1871-2008 historical period, an interannual filter keeping periods between ~2 years and ~7 years has been applied (see Izumo et al. 2014 for details). Significance tests and intervals of confidence are given at the 90% level, and computed using usual two-sided Student t-tests.

2.2) The linear Continuously Stratified ocean model and SST equation

The LCS model allows us to avoid the complexity of a general ocean circulation model, without losing the essential physics to realistically simulate thermocline depth and zonal current variability (the two variables that matter most for ENSO-related SST variations). While shallow water models have some limitations, especially for simulating zonal currents in the western-central Pacific (e.g., Perigaud and Dewitte 1996), models with two (or more) baroclinic modes, such as the LCS model, perform significantly better (Chen et al. 1995, Boulanger and Menkes 2001, Shu and Clarke 2002). LCS models were initially developed by McCreary (1980, 1981) for the equatorial Pacific and then for the equatorial Indian Ocean (e.g. Moore and McCreary 1990). They are based on an expansion of the linearized equations of motion into vertical modes, in order to solve shallow water equations separately for each vertical mode (see e.g. McCreary et al. (2007) for details).

We use here an Indo-Pacific configuration with 0.5° horizontal resolution, derived from Suresh et al. (2013) Indian Ocean configuration. The coastline is defined from the 200m isobaths of ETOPO5 bathymetry. The Indonesian Throughflow (ITF) is similar to McCreary et al. (2007). Background vertical modes are derived from the average equatorial Indo-Pacific region (30°E - 75°W , 10°N - 10°S) World Ocean Atlas 2009 (WOA09; for depth $z < 1500\text{m}$) and Levitus (for $z > 1500\text{m}$) climatological temperature and salinity, a choice close to McCreary et al. (2007). Our results are not very sensitive to changes in background stratification (e.g., using tropical Pacific only or Indian Ocean only). With our choices, the 1st baroclinic mode Kelvin wave speed is $c=2.5$ m/s, and that for the 2nd mode is $c=1.5$ m/s. The horizontal viscosity is $3 \times 10^3 \text{ m}^2 \text{ s}^{-1}$, as in McCreary et al. (2007), adequate for equatorial dynamics (cf. their discussion). A vertical mixing coefficient of $4 \times 10^{-8} \text{ m}^2 \text{ s}^{-3}$, corresponding to a 5 years damping scale for the first baroclinic mode and a 2 years damping scale for the second baroclinic mode is used (i.e., an intermediate value between $0.38 \times 10^{-8} \text{ m}^2 \text{ s}^{-3}$ used by McCreary et al. 2007 and $10 \times 10^{-8} \text{ m}^2 \text{ s}^{-3}$ used by Shu and Clarke 2002). We used the first five vertical modes, although the first two modes dominate the equatorial ocean response at intraseasonal to interannual timescales (e.g. Han et al. 2005).

The LCS model described above simulates thermocline depth and surface current anomalies, but not SST. We use a simple linear SST equation as in many other studies using intermediate models (e.g., Zebiak and Cane 1987, McGregor et al. 2009). The SST equation used here is close to the one of Izumo et al. (2010) with some improvements:

$$\frac{dSST'}{dt} = -U' \frac{d\overline{SST}}{dx} - V' \frac{d\overline{SST}}{dy} + \gamma H' - \alpha SST' \quad (1)$$

The horizontal advection term is approximated by the horizontal advection of climatological observed SST (\overline{SST}) gradients by the LCS anomalous currents U' and V' averaged over the first 100 meters: $-U' \frac{d\overline{SST}}{dx} - V' \frac{d\overline{SST}}{dy}$. Zonal advection dominates the meridional advection (not shown, see also for exemple Vialard et al. 2001). We use the long-term mean SST gradient for simplicity, as using a seasonally-varying gradient gives almost similar results (not shown). The $\gamma H'$ term (H' is the thermocline depth anomaly obtained from the LCS sea surface height anomaly as $H'=150$ SSH') parameterizes the vertical physics, i.e. the interannual modulation of mixing and upwelling by thermocline depth anomalies. The coefficient γ is constant to the east of 140°W ($\gamma = 0.0077$ °C/m), and linearly decreases till one fifth of its maximum value at the western boundary of the Pacific, as in McGregor et al. (2009). This mimics the decreasing effect of the upwelling as the climatological thermocline deepens towards the west. This parameterisation performs as well as the one of Izumo et al. (2010) and Dayan et al. (2014b) for Niño3.4 SST, but performs better for the western Pacific. Heat fluxes are parameterised as a Newtonian damping $-\alpha SST'$, with the associated damping timescale $\alpha^{-1}=2$ months, close to values used by Burgers and Van Oldenborgh (2003), McGregor et al. (2009) and Burgers (2005). To numerically solve equation (1), we take advantage of the fact that α does not vary with time and that the first three terms on the right hand side of equation (1) are independent of SST' , so that we have an analytical formula for the SST' solution:

$$SST' = e^{-\alpha t} \int_{t=0}^{t=t} \left(-U' \frac{d\overline{SST}}{dx} - V' \frac{d\overline{SST}}{dy} + \gamma H' \right) e^{\alpha t} dt \quad (2)$$

We carried out many sensitivity tests by varying the parameters in SST equation (α , γ , climatological mean vs interannually-varying SST (cf. section 2.3), etc...) and found that our results are weakly sensitive to different values of these parameters used in the literature.

2.3) LCS model and SST equation validation

In order to validate our simple ocean model, we ran a control experiment forced by ERAI wind stresses during 1979-2013. We here mainly focus on the validation of the western-central equatorial Pacific (Niño4_{eq}), a critical region for the Bjerknes feedback, and on Niño3.4 SST, the classical ENSO index.

Previous studies (e.g. Vialard et al. 2001) have indicated that zonal advection dominates SSTA in the central-western Pacific, and that vertical processes dominate SSTA in the eastern Pacific.

Fig. 2 hence validates interannual anomalies of U and SST for the western-central Pacific (top panels) and of SSH (or H) and SST for the eastern Pacific (lower panels). The simulated near-surface zonal current anomalies U in the central-west Pacific are in good phase agreement with observations (correlation of $r \sim 0.8$, Fig. 2a) but the amplitudes are somewhat larger. SST near the warm pool eastern edge (e.g. in « Niño_{4eq} ») is also well simulated ($r = 0.80-0.84$, Fig. 2b), despite an overestimation of the SST maxima during the extreme El Niños of 1982-83 and 1997-98. This SST overestimation is related to the use of the climatological SST gradient instead of the interannually-varying observed SST gradient (cf. blue line in Fig. 2b). Here, as we focus on sensitivity experiments that simulate modest SST anomalies, we kept the simple linearization of equation (1). The model reproduces SSH and H variability in the central-east Pacific very well ($r \sim 0.8$, Fig. 2c) resulting in a very accurate simulation of Niño_{3.4} SSTAs ($r \sim 0.9$, Fig. 2d). To summarize, the LCS combined with a simple linear SST equation allows us to simulate the interannual variations of U, H and SST along the equatorial Pacific reasonably well, making it a suitable tool for our study.

2.4) AGCM experiments

We only provide a brief summary of the AGCM experiments used in this paper and refer to Dayan et al. (2014b) for a detailed description. The ECHAM AGCM (Roeckner et al. 2003) is developed at the Max Planck Institute for Meteorology. The version used here is ECHAM 5.4 with a T106 (1.125°) horizontal resolution and 31 hybrid sigma-pressure levels. A mass flux scheme is employed for shallow, mid-level and deep convection (Tiedtke, 1989). ECHAM5 is a widely-used model, having realistic ENSO atmospheric teleconnections (e.g. Dayan et al. 2014b).

The IOD+IOB experiments were forced by a SST pattern representative of a strong IOD event followed by a strong IOB event. This SST pattern was obtained from a lag-regression of daily SST, from previous June 1st to next year's May 31st, on the September-November (SON) DMI standardised value, so as to provide a daily forcing for the AGCM. This pattern is representative of the typical evolution of the IOD, from its onset to its demise. The regression coefficients were then multiplied by two to represent a strong IOD event. The AGCM experiment was forced by this SST pattern, applied in the Indian Ocean only. Since the IOD and ENSO have a tendency to co-vary, this SST forcing also includes a clear IOB signal in winter-spring (Fig. 1b). Two sets (positive and negative IOD) of 20 members ensemble have been run. Here, we mainly exploit their difference, $(nIOD - pIOD)/2$, in order to focus on the symmetric impact of a strong negative (or positive) IOD+IOB event. The wind patterns from these experiments are realistic in the

Indian Ocean (Fig. 1; for more details, see also Dayan et al. 2014b, who did a similar set of IOD experiments). In the Pacific, it is difficult to validate the IOB-forced wind pattern (Fig. 1b) with observations. Indeed, as the IOB and ENSO are highly correlated, the wind response in the western Pacific in observations is also strongly influenced by Pacific variability and cannot easily be compared with our experiment with only anomalies applied in the Indian Ocean sector. We can however note that similar atmospheric responses to the IOB have been found in previous studies with other models (e.g. Annamalai et al. 2005, 2010, Ohba and Ueda 2007, Yamanaka et al. 2009, Santoso et al. 2012). This experiment will be used in section 4.

A longer “PACLIM” 7-members ensemble forced by climatological Sea Surface Temperature in the tropical Pacific Ocean and observed interannually-varying daily SST (ERA-Interim SST from 1982 to 2010) elsewhere was also run (again, see Dayan et al. 2014b for details). It produces significant ensemble-mean equatorial τ_x interannual anomalies over the equatorial western-central Pacific. This experiment will be used in section 5.

3) Estimating the SST response to time-dependent wind forcing

3.1) Introduction to the approach in this paper

In this section, we will explore which temporal variations of zonal wind stress (i.e. “fast” or “slow”) are most efficient to induce a large SST response, especially in the central Pacific. Since the ocean tends to integrate the atmospheric forcing, a very high-frequency wind forcing is not efficient to generate an oceanic response in the equatorial band. At the other end of the spectrum, a wind forcing developing very slowly will permanently be partly balanced by the zonal pressure gradient, with the ocean in a quasi-stationary state (the so-called “fast wave” limit, e.g. Neelin et al. 1991). The ocean hence acts as a bandpass filter of the atmospheric forcing. While the basin modes approach (e.g. Cane and Sarachik 1979, McCreary and Moore 1981) is a good tool to understand the response to periodic forcing in terms of the basin-crossing times of the main oceanic waves (e.g. the equatorial waveguide acts as a kind of band-pass filter in the period range $T \sim 0.5-1$ year, as inferred from the Fourier transform of the impulse response presented below; not shown), it is not really appropriate to understand the response to forcing associated with climate modes such as the IOD or IOB, which are not periodic but rather associated with individual events.

Here, we will exploit the quasi-linear behaviour of equatorial ocean large-scale dynamics (at intraseasonal to interannual timescales) to describe the oceanic response to any time-dependent forcing as a function of the impulse response to a single wind stress “pulse”. In

section 3.2, we will remind what is the oceanic response to such wind “pulse” in the western Pacific. In section 3.3, we will show that the equatorial ocean acts as a “causal band-pass filter”¹ of $\tau_x(t)$, i.e. that SST anomalies can be estimated from changes in seasonally-averaged wind stress over the past ~ 8 -10 months. We will then demonstrate the validity of this method by applying it to reconstruct observed SSTs in Niño_{4eq} from wind stress past evolution. In section 3.4, we will apply this approach to a wind anomaly in the western Pacific, typical of the Pacific wind stress response to Indian Ocean (IOD and IOB) SST anomalies.

3.2) Delayed negative feedbacks in an ENSO-like « pulse » experiment

We first present the response to a wind stress pulse with “ENSO-like” spatial pattern (i.e. westerly pulse in the *central-western* equatorial Pacific). The pulse lasts 10 days (sufficiently shorter than the oceanic response) with a Gaussian spatial pattern represented by $\tau_x = A \exp(-(((x-x_0)/\Delta x)^2 + (y/\Delta y)^2)/2)$, with $\Delta x = 25^\circ$, $\Delta y = 7^\circ$, $x_0 = 180^\circ$ and $A = 0.1 \text{ Nm}^{-2}$ (so that the integral of this pulse is $1 \text{ Nm}^{-2}\text{day}$, so as to be an approximation of a Dirac). The Δx , Δy and x_0 parameters have been chosen in order to match the spatial pattern of ERAI zonal wind stress regressed on Niño_{3.4} (not shown). This experiment will be useful to validate the convolution/causal-filter approach for ENSO-related SST variability.

Figs 3a,b,c show zonal-time sections of the equatorial ocean response to this ENSO-like westerly pulse. It shows the well-known response to a westerly wind burst, with a downwelling Kelvin wave and an upwelling Rossby wave being forced. The anomalous eastward current and deep thermocline associated with those waves contribute to a SST warming in the central Pacific during the initial 2-3 months. The downwelling Kelvin wave reflects as a downwelling Rossby wave at the eastern boundary, associated with weak positive SSH and strong negative U anomalies, that tends overall to cool the SST through zonal advection. This is the delayed negative feedback emphasized in the zonal advective-reflective model of Picaut et al. (1997). The upwelling Rossby wave to the west reflects as an upwelling Kelvin wave at the western boundary, which weakly contributes to negative anomalies in SSH and U that also tend to cool the SST. This is the delayed negative feedback associated with the delayed oscillator described by Schopf and Suarez (1988) and Battisti and Hirst (1989). There is a lag of about half a year between the initial warm SST response and the delayed SST cooling.

¹ We use the « causal band-pass filter » term to traduce the fact that the oceanic response integrates wind stress variations over the last couple of months.

Figure 3d shows the Niño4_{eq} SSTA response to this wind impulse (hereafter $R_{\text{pulse}}(t)$). This impulse response can be approximated as an initial constant warming that lasts 3 months and a delayed cooling, weaker but longer, that lasts 4 months (dashed curve on Fig. 3d¹, hereafter $R'_{\text{pulse}}(t)$). In the following subsection, we will demonstrate that the response to any time-dependent wind forcing with the same spatial pattern can efficiently be approximated using this idealised shape of the oceanic impulse response.

3.3) Resulting transfer function between wind and SST response

Thanks to the linearity of the LCS and SST equation, the response of a field $F(x,y,t)$ (such as SST, U, or SSH) to any $\tau_{x,cp}$ temporal variations in the central-west Pacific (with a similar spatial pattern to the idealised ENSO-like Gaussian pulse) can be obtained as a convolution of τ_x to the basis impulse response R_{pulse} (R_{pulse} being the response to an approximated Dirac):

$$F(x, y, t) = \int_{t=-\infty}^{t=t} \tau_{x,cp}(\tau) R_{\text{pulse}}(x, y, t - \tau) d\tau \quad (3)$$

For the Niño4_{eq} box, if one further approximates the $R_{\text{pulse}}(t)$ by the idealised step function plotted in Fig. 3d (dashed red line), the Niño4_{eq} SSTA response to ENSO-like wind stress variations in the central-west Pacific can be approximated as:

$$\text{Niño4}_{eq} \text{ SST}(t) \sim 70 (\tau_{x,cp}^{3m}(t-1.5) - \tau_{x,cp}^{4m}(t-7.5)/2) \quad (4)$$

where t is time (in months), and $\tau_{x,cp}^{3m}$ for instance is the *3 months running mean* τ_x anomaly (in Nm^{-2}) averaged over (140°E - 140°W , 2°S - 2°N). That is, the SST response to El Niño-like wind stress anomalies in the central Pacific can be approximated as the difference between the three-months average of $\tau_{x,cp}$ 1.5 months earlier minus half of the four-months average of $\tau_{x,cp}$ 7.5 (i.e. $6+1.5$) months earlier, scaled by a $70^\circ\text{C N}^{-1} \text{ m}^2$ factor. This transfer function acts as a bandpass filter: 1) due to the running mean smoothing, it favours long-lasting (i.e. \sim seasonal) anomalies; 2) due to the negative feedback, it favours seasonal wind anomalies that change sign over the following ~ 6 months. This transfer function is mathematically known as a “Causal Finite Impulse Response (FIR) filter”, whose spectral response can be computed explicitly and is indeed, for the range of parameters used here, a kind of band-pass filter (e.g. Oppenheim et al. 1983).

¹ Note that to make the approximation quantitatively accurate, the choice of the two boxcar functions (i.e. lagged running-box filters when convoluted) in e.g. Fig. 3d is made so that not only the SST impulse response is well approximated, but also its temporal integral (Fig. 3e): as the impulse response is then convoluted (cf. following section), the area matters actually more than the maximal amplitude of the peaks.

If a different region than Niño4_{eq} or a different wind forcing pattern is used, the general approach remains the same, but the R_{pulse} function (and hence its idealised R'_{pulse} step function approximation) will change. For instance, considering the SST evolution in a « Niño3.4_{eq} » region more to the east (170°W-120°W, 2°N-2°S) leads to slight changes with notably a slightly weaker delayed negative feedback: $\text{Niño3.4}_{\text{eq}} \text{ SST}(t) \sim 75 (\tau_{x,\text{cp}}^{3m}(t-2) - \tau_{x,\text{cp}}^{5m}(t-8)/3)$. For the usual Niño3.4 region, there is an overall decrease, both in amplitude and in the delayed negative feedback, because of the average over a wider 5°N-5°S band: $\text{Niño3.4} \text{ SST}(t) \sim 45 (\tau_{x,\text{cp}}^{3m}(t-2) - \tau_{x,\text{cp}}^{5m}(t-8)/6)$.

In order to check the validity of this method, we now compare the SSTA computed using equation (4) with the SSTA from the LCS control simulation (Fig. 4). The SST estimated from equation (4) correlates almost perfectly with the exact LCS-derived SST for Niño4_{eq} ($r=0.98$, $r^2=96\%$). Since there is a strong correlation between SSTA and wind anomalies in the real world, as the SSTA drive the convective anomalies, this high correlation could have been expected. However, removing the negative feedback (negative step in the R'_{pulse} function) from equation (4) results in a 25% loss of explained variance (significantly weaker $r=0.84$; $r^2=71\%$ only). Hence there is a strong indication that equation (4) captures some of the delayed negative feedback physics inherent to ENSO. Equation (4) however leads to a slight underestimation in amplitude (by 26%), a bias which is reasonable with regards to the several approximations done, and which is possibly partly due to an underestimation of the wind fetch during ENSO (this bias can be easily corrected with a simple linear regression, which estimates a correction factor of 1.34; cf. Fig 4).

A similar equation to (4) can be derived for other parameters than SST, e.g. sea level and zonal current anomalies (Table 1¹). At all locations, the correlation of the causal band-pass filtered $\tau_{x,\text{cp}}$ with observed variables ranges between 0.6 and 0.9. In addition, including the delayed negative feedback systematically improves these correlations. This confirms that the simple approach of equation (4) can be used to estimate the oceanic response to observed El Niño wind stress variations, and that the delayed negative feedback associated with wave reflections plays a non-negligible role in this response.

To summarize, in this subsection we have shown that the complex dynamics associated with equatorial waves and their reflections can efficiently be approximated by computing the

¹ For SST, validating the method with observations is less trivial statistically: because of the strong ocean-atmosphere coupling in the central Pacific, $\tau_{x,\text{cp}}$ is proportional to Niño4_{eq}SST, so that $\tau_{x,\text{cp}}$ itself performs as well as the causal-filtered $\tau_{x,\text{cp}}$, with similar scores (not shown).

oceanic response (in terms of currents, sea level or SST) as a causal bandpass filter of zonal wind stress anomalies. In the rest of this paper, we will use this approach to disentangle the respective influences of IOD and IOB on ENSO onset.

3.4) Transfer function for IOB-like forcing in the western Pacific

The previous subsection did focus on the oceanic response to zonal wind stress anomalies in the central-western Pacific, $\tau_{x,cp}$, related to the dominant ENSO variability. But Indian Ocean SSTAs rather drive wind stress anomalies in the western Pacific (Fig. 1). We will now detail the impulse response and related transfer function of ocean dynamics for zonal wind stress forcing in the *western* Pacific. The “IOB-like” westerly pulse is maximum at the western boundary ($x_0=130^\circ\text{E}$), with a width $\Delta x=30^\circ$. These parameters have been chosen so that the idealised Gaussian pattern shown in Fig. 5b mimics the AGCM wind response to an IOB in JFM (Fig. 1b). The impulse response to IOB-like forcing (Fig. 6) is qualitatively similar to the response to ENSO-like forcing (Fig. 3). There are however small differences: the response is weaker since the western boundary shortens the wind fetch; the initial warming in the central Pacific is shorter because of the earlier reflection of the upwelling Rossby wave at the western boundary; the delayed cooling in the central Pacific has a slightly different longitude-time distribution, because of the different timing of the reflected waves at the eastern boundary. This translates into the following changes in the causal filter approximation :

$$\text{Niño4}_{eq} \text{ SST}(t) \sim 55 (\tau_{x,wp}^{2m}(t-1.5) - \tau_{x,wp}^{4m}(t-7.5)/2) \quad (5)$$

where $\tau_{x,wp}$ is defined as the 130°E - 160°W , 2°S - 2°N zonal wind stress average. In particular, Niño4_{eq} SST variability in late spring, e.g. April-May (AM) can be inferred from a 2 months average of this equation (5), for AM, and thus approximated as:

$$\text{Niño4}_{eq} \text{ SST}(AM) \sim 55 (\tau_{x,wp}(FMA) - \tau_{x,wp}(JASON)/2) \quad (6)$$

This simply means that the temporal evolution of $\tau_{x,wp}$ that matters for late spring Niño4_{eq} SST is the difference between the winter-spring (February-April: FMA) $\tau_{x,wp}$ anomaly and half of previous summer-fall (July-November: JASON) $\tau_{x,wp}$ anomaly.

4) Response to fast and slow western Pacific wind variations

In the present section, we will apply the concepts of section 3.4 to understand the difference in oceanic response between an IOD followed by an IOB (fast wind variations) and a “pure” IOB (slower wind variations in the western Pacific). To that end, we have created two idealised sets of wind stress forcings. In the “FAST” experiment, the wind stress forcing is constructed to

mimic the one diagnosed from the AGCM experiments shown in Fig. 1: we use the idealised IOB-like Gaussian spatial pattern shown in Fig. 5b. The westerly wind appears suddenly on January 1st (with amplitude $A=0.02\text{Nm}^{-2}$) and disappears suddenly on March 31st (red line in Fig. 7a). This idealised temporal evolution crudely mimics the “real” forcing inferred from the AGCM experiments that include both IOD and IOB forcing (black line in Figs 1c and 7a). Fig. 7b shows that the SST response to this idealised forcing (red curve) is very close to the one forced by the actual wind stress evolution diagnosed from the AGCM (black curve), with qualitatively-similar amplitude and timing of the peak in spring (however with a slight overestimation of $\sim 20\%$).

We construct the “SLOW” idealised experiment according to our hypothesis that in the pure IOB case, the wind anomaly in the western Pacific develops more progressively. In this experiment, the western Pacific wind anomaly increases linearly during six months from June (when ENSO, and thus the IOB, usually starts developing) to the following January, when ENSO usually peaks (green curve in Fig. 8a).

The difference in oceanic response between the “FAST” and “SLOW” IOB idealised experiments is illustrated in Figs 8 and 9. In the SLOW experiment, the “pure” IOB induces a $\sim 0.5^\circ\text{C}$ Niño_{4eq} warming peak in winter (February) (Fig. 8). This warming is slightly weaker, and starts decreasing earlier than in FAST, because the delayed negative feedback has time to counteract the initial SST increase. In the FAST experiment, the sudden Pacific wind stress appearance associated with the IOD demise in winter slightly amplifies the SST response in the central Pacific in late spring-early summer. Fig. 9 shows the SST spatial patterns in AMJ. The warming occurs in a narrower equatorial band in the FAST experiment, because the basin had less time to adjust through Rossby waves. The FAST response is stronger in the central Pacific, where the largest FAST-SLOW differences are found (Fig. 9c). The peaks of FAST and of the FAST-SLOW difference are maximum around April-May, a period when the mean equatorial Pacific SST is at its warmest, and thus when the equatorial atmosphere is most sensitive to SST anomalies, making it the most unstable season for El Niño triggering (e.g. Spencer 2004). The FAST-SLOW differences are also maximal in the central Pacific, where convection is most sensitive to SST anomalies thanks to high mean SST (e.g. Palmer and Mansfield 1984). Hence, even if the amplitude of the difference FAST-SLOW is rather weak ($\sim 0.15^\circ\text{C}/2\sigma_{\text{IOD}}$, i.e. $\sim 30\%$ of SLOW-induced maximal warming), there is a potential for these SST anomalies to be amplified by the Bjerkness feedback (see example in e.g. Florenchie and Perigaud 2002), and thus to significantly influence ENSO. Furthermore, the highly-idealised experimental setup used here

may underestimate the IOD effect, as suggested by the following section based on a more realistic setup. We will discuss these points further in section 6.

5) IOD/IOB relative influences in a more realistic experiment

In this section, we will use the more realistic PACLIM experimental setup to test the hypothesis that the IOD amplifies the IOB tendency to induce an ENSO transition and to more accurately quantify IOD and IOB respective influences. We will first use a partial correlation method (section 5.1), and then a composite analysis (section 5.2) to separate the IOD and IOB influences on central Pacific wind and SST changes. We will then identify the observed SST and related precipitation patterns in the Indian Ocean that are most associated with those changes (section 5.3).

5.1) Separating IOD/IOB influences using partial correlation

The AGCM “PACLIM” 7 members ensemble experiment was forced by interannually-varying observed SST during 1982-2010 except in the tropical Pacific where SST was kept climatological (cf. section 2). Wind variations associated with tropical Pacific ENSO SST anomalies are thus filtered out from this experiment, but IOD and IOB-induced wind variations over the Pacific remain and can hence be more easily identified and statistically separated. The LCS model was then forced by winds from the PACLIM experiment over the Pacific, in order to quantify the SST impacts of these IOD/IOB wind variations (Fig. 5a).

Figs 10 and 11 illustrate the respective influences of the IOD and IOB on the temporal evolution of western Pacific $\tau_{x,wp}$ and Niño4_{eq} SST anomalies. In these figures we use a partial correlation method to statistically separate the effects of “pure” IODs (i.e. without IOB) and “pure” IOBs (i.e. without IOD) on τ and SST variations (using a multiple linear regression gives similar results; not shown). “Partial regression” coefficients, noted a for IOD and b for IOB, are further obtained by multiplying these partial correlation coefficients by the standard deviation of the field of interest (here τ or SST). Figs 10 and 11 show the partial regression coefficients $-a$ for a “pure” nIOD and $-b$ for a “pure” nIOB, while their sum $-a-b$ illustrates the “nIOD+nIOB” case.

Similarly to previous studies (e.g. Shinoda et al. 2004a, Zhao and Nigam 2015), Fig. 10 illustrates that, when the IOB signal is properly removed, the “pure” IOD signal mostly appears as a monopole in SST in the eastern Indian Ocean in summer-fall (JASON, Fig. 10a), that has largely disappeared the following winter (FMA, Fig. 10b). As can be expected from the Gill (1982) model, this drives an easterly wind response in summer-fall in the western Pacific (Fig.

10a, 11a), that has largely disappeared by the following late winter/spring (Fig. 10b, 11a). The IOB signal, on the other hand, appears as a progressive cooling (or warming) of the entire Indian ocean, still weak in JASON (Fig. 10c) but that culminates in FMA (Fig. 10d). As expected from the Gill model, the western Pacific response is a westerly wind anomaly that is still weak in JASON but that culminates in FMA the following year (Figs 10c,d and 11a). Finally, the combined occurrence of an IOD and IOB displays a SST signal in both the eastern and western poles in JASON (Fig 10e), but this signal becomes very similar to the pure IOB uniform signal in FMA (Fig. 10f) due to the sudden IOD disappearance. As a result, there is no wind anomaly in the western Pacific in summer-fall (Fig. 10e), due to the cancelation of signals forced by the opposite eastern and western Indian Ocean poles as discussed by Annamalai et al. (2005, 2010). On the other hand, the FMA western Pacific wind response to the IOD+IOB is very similar to that of the pure IOB (Fig. 10df), due to the fast disappearance of the IOD.

The Niño_{4eq} SST responses to these IOD or IOB wind evolutions both display a statistically significant Niño_{4eq} warming in spring in the central Pacific (Fig. 11c). These SST responses are very well captured by the causal-filtered wind stress derived from equation (5) (compare Fig. 11b and 11c). Equations (5) and (6) indicate that the wind change over ~6 months is as important as the actual absolute value for generating a SST response in Niño_{4eq}. This explains why the IOD contribution is not negligible compared to the IOB one, despite its smaller absolute wind stress signature in winter-spring (Figs 10 and 11). The “pure” IOD influence ($-a \approx 0.57 \pm 0.3^\circ\text{C}$ for spring SST) is highly significant. It is somewhat weaker than the “pure” IOB one ($-b \approx 0.97 \pm 0.15^\circ\text{C}$; $a/b \approx 60\%$; Fig. 11c), although the difference between the IOD and IOB-induced SST responses is not statistically significant at the 90% confidence level.

The results from combined “nIOD+nIOB” and pure “nIOB” cases are qualitatively similar to the results from the idealised FAST and SLOW experiments, but with 1.2 to 3 times larger SST signals. These amplitudes however decrease, becoming quantitatively closer to (but still larger than) the results of the idealised experiments, if the extreme El Niños of 1982-83 and 1997-98 are removed from the regression analysis (not shown), possibly because of non-linearities in the AGCM response to SST (e.g. Ohba and Ueda 2009, Ohba et al. 2010, Ohba 2012).

5.2) Separating IOD/IOB influences using composites

Figure 12 offers an alternative way to separate IOD and IOB signals, using a composite analysis of pure “IOD”, “IOB” and “IOD+IOB”, complementary to the partial regression discussed in section 5.1. Pure IOD and IOB events and combined IOB/IOD events are defined using 0.65

standard deviation threshold of the indices over the 29 years of the PACLIM experiments. Our results are however not very sensitive to the selection criterion: using a threshold of 1 gives qualitatively similar result (not shown). The statistical significance of the results obtained from the composites analysis is considerably enhanced by the ensemble of seven members performed for PACLIM experiment: a composite on e.g. three events indeed results in an average of 21 members for the AGCM, as for the LCS forced by the AGCM.

Figure 12 summarizes results from this composite analysis. We do not show the composites for negative and positive IODs / IOBs separately, because the asymmetries are not statistically significant (as discussed in Dayan et al. 2014), and we hence show the difference of negative and positive events (we will however discuss potential asymmetries in section 6). There are 9 pure IOB events (i.e. ENSOs that did not trigger an IOD event, with SST signals similar to those of Fig. 10cd) in observations over 1982-2010 (using ERAI SST; 27 over 1871-2010 using interannually-filtered HadiSST). There are 6 pure IOD events over 1982-2010 (17 over 1871-2010), with a SST pattern that tends in summer-fall to be closer to a monopole near Sumatra/Java as on figure 10a rather than to a dipole as on e.g. Fig. 1a. Shinoda et al. 2004a showed that those events are those that occurred independently of ENSO.

In those composites, the Niño4_{eq} SST response in late spring is again well approximated by equation (6), being close to $55 (\tau_{x,wp}(FMA) - \tau_{x,wp}(JASON))/2$ (Fig. 12). The SST response inferred from this composite analysis is coherent with the partial correlation analysis of figure 11. Pure IOD and pure IOB events produce a similar SST anomaly in spring in the central Pacific (with the IOD central Pacific SST response being of ~85% of the IOB influence), with the IOD+IOB case being statistically significantly stronger than the pure IOB case. This suggests again that the IOD significantly contributes to generate SST anomalies during the following spring in the central Pacific.

Overall, the set of more realistic experiments (PACLIM) agrees with our earlier idealized FAST and SLOW experiments in suggesting that the IOD enhances the spring warming in the central Pacific remotely driven by the Indian Ocean, and clarifies the IOD and IOB respective roles. This enhancement of the central Pacific SST response is however stronger in the more realistic (PACLIM) experiments, being of $\sim 0.6^\circ\text{C}/2\sigma_{\text{IOD}}$, i.e. ~60-85% of the influence of a pure IOB with the same standardized amplitude.

5.3) SST/precipitation patterns causing $\tau_{x,wp}$ seasonal change

Equation (6) relates the central Pacific warming in spring with $\tau_{x,wp}$ wind change between previous JASON and FMA, precisely with $\tau_{x,wp}$ seasonal change FMA-JASON/2. To identify the actual cause of this $\tau_{x,wp}$ change (which is the forcing on the ocean that will induce a strong warming in spring in the central Pacific), Fig. 13 shows the regression of the FMA-JASON/2 change in SST, precipitation and wind PACLIM ensemble mean on the FMA-JASON/2 change in western Pacific $\tau_{x,wp}$. The clearest pattern is a SST decrease in the eastern Indian Ocean and maritime continent, i.e. a disappearance of the nIOD eastern pole as expected during a transition from a negative IOD in JASON to an IOB cooling in FMA. This SST decrease is associated with physically-coherent changes (see also e.g. Hendon 2003) in precipitation (reduced rain over the IOD eastern pole) and winds (wind divergence associated with the SST decrease and reduced precipitation). As a result, westerly wind anomalies develop in the western Pacific (further amplified by a local atmospheric positive feedback with a precipitation increase maximal in the SPCZ, likely due to wind and moisture convergence there; cf. Fig. A2 of Watanabe and Jin 2002).

Overall, this figure hence confirms our working hypothesis: the difference FMA-JASON/2 in western Pacific $\tau_{x,wp}$, at the origin of spring Niño_{4eq} SST variability, is remotely forced in PACLIM both by IOD disappearance and IOB appearance.

6) Summary and discussion

6.1) Summary

In this study, we have derived a simple relation between SST anomalies in the equatorial Pacific and zonal wind stress changes over the preceding months. This approach is useful to identify the actual physical causes of observed oceanic anomalies and is applied to understand the respective influences of the IOB and IOD SST anomalies on ENSO through atmospheric teleconnections.

To capture the essence of the linear response to varying winds and to derive the above-mentioned simple relation, we have used a linear continuously-stratified (LCS) ocean model combined with a linear SST equation forced by observed zonal wind stresses. This model reproduces observed equatorial Pacific SST, sea surface height and zonal current anomalies reasonably well. The linearity of the model allows the ocean response to any temporal evolution of a given wind stress spatial pattern to be computed exactly as a temporal

convolution of this wind evolution to the impulse response (i.e. the response to a pulse with the same wind pattern). This property can be exploited to estimate the model SST (or zonal current or surface height) anomaly from the past evolution of wind stress. This relation takes the form of a « causal band-pass filter » of zonal wind stress:

$$SST \approx C \left(\int_{P1} \tau_x dt - c \int_{P2} \tau_x dt \right) \quad (7)$$

where $P1$ and $P2$ are two successive periods, lasting a couple of months each and separated by about 6 months, $0 < c < 1$, and C is a scaling factor. The first term in the equation represents the fast oceanic response, while the second represents the delayed negative feedback associated with wave reflection at both boundaries. When $P1$, $P2$, c and C are tuned to represent the response to an ENSO-like wind stress forcing (equation 4), this equation is able to reproduce observed variations in the central equatorial Pacific reasonably well (Fig. 4 and Table 1).

We have further used this method to understand the respective IOD and IOB influences on following year's ENSO state. Idealised AGCM experiments forced by the combined IOD+IOB patterns suggest that atmospheric responses associated with the IOD eastern pole and IOB-related western pole cancel until the end of fall (in agreement with previous studies by Watanabe and Jin 2002, Annamalai et al. 2005, Ohba and Ueda 2007, Annamalai et al. 2010). The quick IOD disappearance then induces a fast growth of IOB-forced zonal wind stress anomalies in the western Pacific. We have then performed two idealised experiments, with SLOW (IOB-only) or FAST (IOD+IOB) developing wind stress anomalies of the same amplitude in the western Pacific. Those experiments suggest that the IOD strengthens the “pure” IOB SST warming in the central Pacific in late spring by about 30% (i.e. $\sim 0.2^\circ\text{C}/2\sigma_{\text{IOD}}$).

The statistical analysis of a longer and more realistic experimental setup, “PACLIM”, with the ocean model being forced by wind stresses from an AGCM experiment with climatological SST within the tropical Pacific but observed daily SST elsewhere, is qualitatively consistent with the idealised simulations above. In this experiment, the absence of the ENSO signal allows us to more easily disentangle the relative roles of the IOD and IOB (both correlated to ENSO) through partial correlation and composite analyses. This analysis suggests that the IOD-induced signal could be actually stronger, being of about 60-85% (i.e. $\sim 0.6^\circ\text{C}/2\sigma_{\text{IOD}}$) of the IOB-induced SST signal in the central Pacific in spring. This analysis also indicates that “pure IOD” cases (i.e. IODs that occur independently of ENSO and of an IOB, with essentially an eastern pole SST anomaly) can also generate a SST response in the central Pacific. Equation (6) further allows identifying SST and rainfall changes over the IOD eastern pole and maritime continent,

from previous boreal summer-autumn to next winter-spring, as the most important factors for driving a SST response in next spring in the central Pacific (Fig. 13).

To sum up, the IOB dominates the western Pacific winter-spring windstress response to the Indian Ocean. But if an IOD occurs, it will contribute to opposite wind anomalies during the previous summer-fall (cf. Fig. 10). This will thus increase the summer-fall to winter-spring wind change and thus amplify the SST response in the central Pacific during late spring (where and when the sensitivity of the coupled system is at its strongest). The PACLIM experiment suggests that the IOD-induced central Pacific SST signal is ~60-85% of the pure IOB signal. This IOD influence, more “ENSO-independent” than the IOB influence, could explain physically why the IOD has statistically a significant influence on ENSO onset predictability in observations and climate models (cf. following discussion in section 6.2). To conclude, the present study reconciles apparently-contradictory previous studies, and recommends applying such a convolution approach when investigating any potential external influence on an equatorial ocean.

6.2) Discussion and perspectives

The present results suggest that the IOB has a stronger influence on Pacific SST than the IOD. This may seem contradictory to previous studies, which suggest that the IOD is a better predictor of ENSO than the IOB (Izumo et al. 2014, Dayan et al. 2014a, Jourdain et al. 2015). However, the IOD is more independent of ENSO than the IOB ($r^2_{\text{DMI-ENSO}} = 48\%$, $r^2_{\text{IOB-ENSO}} = 71\%$ from interannually-filtered HadISST data over 1871-2010). The IOB is thus a more systematic response to ENSO and feedbacks on it in a quite systematic way: the IOB influence may hence be seen as part of the ENSO cycle. On the other hand, the more independent IOD offers an additional degree of freedom, a partly-external influence on ENSO that can be exploited to improve ENSO forecast (Izumo et al. 2014).

Results discussed in the present study allow us to reconcile some apparently contradictory results published earlier. Regarding the mechanism explaining the IOD influence on following year ENSO, Izumo et al. (2010) were underlining the role played by the rapid termination of the IOD eastern pole and related rapid change of wind over the Pacific at the end of the IOD, but were arguing through partial correlation analysis that the eastern pole of a nIOD forces an easterly anomaly over the Pacific during the IOD (independently of ENSO), that quickly collapses in early boreal winter. This agrees with the most realistic PACLIM setup of section 5 (and with Annamalai et al. 2010), which suggests that “pure” IOD events (i.e. mainly a SST

signal near Java-Sumatra, Fig. 10a) significantly impact $\tau_{x,wp}$ in summer-fall (Figs 10 and 11). But this may appear at odd with the more idealized IOD experiments of section 4 (and with Dayan et al. 2014b ones), which show that there is no remotely-driven wind easterly anomaly over the Pacific in summer-fall during a typical IOD (i.e. an IOD that co-occurs with an IOB, in which case the effect of the eastern and western poles of the IOD cancel out, as suggested by Annamalai et al. 2005a), but only westerly anomalies developing later in winter-spring. This apparent discrepancy can simply be explained by the difference in SST forcing patterns. The forcing pattern of the idealized IOD AGCM experiment is obtained through a *simple* regression on the IOD index, and results in SST anomalies both in the eastern (“pure” IOD pattern) and western (IOB signature) Indian Ocean (Fig 1a), because of the tendency of IODs to co-occur with ENSO (and hence with the IOB). On the other hand, the “pure IOD” SST anomalies (Fig. 10a) that force PACLIM, inferred from a *partial* regression, are dominated by the eastern pole, and are thus associated with a wind response over the Pacific in summer-fall. The IOD hence induces an increase of the western Pacific zonal wind seasonal change from boreal summer-fall to winter-spring (Figs. 10, 11, 12), and consequently a larger SST response as shown by equations (5) and (6). By underlining that the important factor to drive the SST change in the central Pacific in spring is not only the exact sign of the wind during winter-spring, but also the wind change between boreal summer-fall and winter-spring, the present study hence reconciles previous studies emphasizing the IOB influence with Izumo et al. (2010).

Another possible mechanism suggested for the IOD influence on ENSO is an oceanic bridge, via the ITF (Yuan et al. 2011). Several previous studies have suggested that this bridge is weak (Clarke 1991), since most of the IOD-forced equatorial Kelvin wave energy is reflected in Rossby wave energy at equatorial Indian Ocean eastern boundary along Sumatra island, leaving only little energy for wave propagation through the Indonesian Seas to the Pacific. This bridge seems indeed negligible in comparison with the atmospheric bridge (Schwarzkopf and Boening 2011). To verify this here, we can use the LCS model, as McCreary et al. (2007) demonstrated that, in a configuration close to the one we use in the present study, it could reasonably reproduce ITF dynamics. We have thus run a PACLIM-forced LCS experiment similar to the one mainly shown in Fig. 11c, but forced by Indian Ocean wind stresses instead of Pacific ones, to isolate the oceanic bridge effect (light blue curve in Fig. 11c). As seen on Fig. 11c, our results suggest that the effect of the oceanic bridge on central Pacific SST is very small relative to the one expected from the atmospheric bridge. Even a large decrease in horizontal viscosity ($500 \text{ m}^2\text{s}^{-1}$ instead of $3000 \text{ m}^2\text{s}^{-1}$) does not yield considerable increase in the oceanic

bridge contribution (only by $\sim 30\%$; not shown), suggesting that the results of the present study are robust in this setup. Our experiments thus agree with most previous studies in designating the atmospheric bridge as the main path for an influence of the Indian Ocean on the Pacific at interannual timescales.

Concerning the robustness of the results, changes in horizontal resolution (from 0.5° to 0.25°), details of the coastline, mean vertical stratification and horizontal viscosity of the linear ocean model do not qualitatively affect the conclusions of the present study. Hence, the present results should not change substantially with other realistic oceanic models. On the other hand, concerning the AGCM experiments, previous studies have indicated that the Pacific wind response to Indian Ocean SST anomalies could also depend of the inclusion of maritime continent SST anomalies (which would strengthen IOD eastern pole influence; Annamalai et al. 2010) and to the atmospheric model mean state (Watanabe and Jin 2002). We did additional idealised IOD experiments by including SST anomalies in the maritime continent region (the ones used in Dayan et al. 2014b) and obtained very similar results to the ones described in section 4. Concerning ECHAM AGCM mean state, its biases could affect our results. Prodhomme et al. (2013) noted that, in an almost similar configuration to the one here, ECHAM underestimates deep atmospheric convection in fall-winter over the eastern Indian Ocean and maritime continent and overestimates it over the southwest Indian Ocean with a too strong ITCZ (two rather “classical” biases in AGCMs; Bollasina and Ming 2013). As a result, our AGCM experiments might underestimate the atmospheric response to the IOD eastern pole and overestimate the response to IOD western pole in fall and to the IOB in winter, as suggested from Figs 3 and 11 of Dayan et al. (2014b). It is of course not obvious to anticipate how these biases may influence our results, and the safest way to address this question is to investigate it in other AGCMs.

Many recent studies (e.g. Ohba and Ueda 2009a; Ohba et al. 2010; Ohba 2013) show that the transition process of ENSO is asymmetric. Dayan et al. (2015), using the same AGCM as here, investigated the asymmetry of the AGCM wind stress response over the Pacific to IOB forcing by performing ensembles of this AGCM forced by either a negative or positive IOB pattern. They only found a weak asymmetry of the same sign as in the aforementioned studies (i.e. an IOB warming forces a slightly stronger wind stress response over the Pacific than a cooling), which was however not statistically significant (see Dayan et al. 2015 for more discussion; we have found the same result in our slightly different idealised IOD experimental setup). Analysing asymmetries using the composite technique discussed in section 5.2 suggest that

these asymmetries derived from the more realistic PACLIM experimental setup are again weak and not statistically significant at the 90% level, for the various pure IOD, pure IOB or IOD+IOB cases (not shown). It is however a must to ascertain these results using a modelling setup similar to PACLIM experiment but with other AGCMs and a large number of members.

Our simple approach to determine the oceanic response to past wind stress changes from a simple delayed feedback equation can be pretty useful for idealised studies. Although we have only applied this approach to a wind spatial pattern that does not vary in time in the current paper, this approach could be extended to any spatial pattern of equatorial τ_x , and thus to any wind spatio-temporal evolution (cf. Appendix for a crude extension towards this), by first computing impulse responses to pulses all along the equatorial band (this would then be formally viewed as determining the “Green’s function” for the oceanic response to windstress, in a somehow similar strategy to Barsugli and Sadershukh 2002). It could also be applied to other equatorial basins. Such an approach that allows determining a simple relation between the SST response and past wind stress changes can be very useful, notably in air-sea interactions studies.

Acknowledgements: we would like to thank Dr. Sébastien Masson, funded by the Conseil National des Astronomes et Physiciens (CNAP), who helped us in setting up and running the AGCM experiments. We would also like to thank the three reviewers for their helpful comments, that have well improved the manuscript and especially its clarity. Takeshi Izumo, Jérôme Vialard and Matthieu Lengaigne, funded by IRD, gratefully acknowledge the National Institute of Oceanography (NIO, Goa, India) for hosting them during their stays there, and would like to thank Dr. A.S. Unnikrishnan and his colleagues at NIO for their hospitality and help. Hugo Dayan was funded by a PhD grant of Ministère de l’Enseignement Supérieur et de la Recherche, by the Institut National des Sciences de l’Univers (INSU) LEFE program and by the Agence Nationale pour la Recherche ANR-10-Blanc-616835 METRO project. The NOAA, NCEP, CPC and IRI climate data libraries, and ECMWF ERAI data, were notably used here. This is NIO contribution XXXX.

APPENDIX

Estimating the oceanic response to any equatorial $\tau_x(\mathbf{x},t)$

Equation (4) can also be written for SSH or U or for other averaging regions. And the convolution approach can be generalised to the response at any longitude to an equatorial τ_x forcing at any longitude, without losing too much simplicity. One just needs to take into

account the longitudinal variations in the temporal constants used in the equations of causal-filters given in section 3. These longitudinal variations are related to Kelvin and Rossby waves characteristics, propagation speed, attenuation and interference between them for the (mainly) first and second baroclinic modes. To precisely obtain them, one could force the LCS by various spatial pulses distributed along the equatorial Pacific (i.e. formally determining the “Green’s function”), to reconstruct the whole response and to see the sensitivity of the response to longitude. Here the main purpose of this section is simpler: give very simplified equations for the “causal filtering” approximation of the oceanic response at *any* longitude to *any* equatorial $\tau_x(x_f, t)$ forcing. These crude equations are inferred from the impulse responses to western, central-west (described in section 3) and central-east Pacific (not shown) westerlies, and need to be precised in future studies.

So, as a very crude approximation of the oceanic response estimated from the LCS model plus SST equation, we can write a semi-empirical formula for the linear oceanic response of the oceanic field $F_{eq}(x, t)$ (average over 2°N-2°S) to any $\tau_x(x_f, t)$ forcing along the equator:

$$F_{eq}(x, t) = C \int_{x_f=x_w}^{x_f=x} \left(\left(1 - \frac{x-x_f}{x_E-x_f} \right) \tau_x^{m_1} \left(x_f, t - t_0 - \frac{x-x_f}{c_K} \right) - \frac{1}{2} \left(1 - d_1(x, x_f) \right) \tau_x^{m_2} \left(x_f, t - t_0 - x_E - x_f c_{K/R} - x_E - x c_{R/d} x_f + C x_f = x x_f = x_E \quad 1 - x_f - x x_f - x_W \quad \tau_x \quad m_1 x_f, t - t_0 - x_f - x c_R - \frac{1}{2} \right. \right. \\ \left. \left. 1 - d_2(x, x_f) \quad \tau_x \quad m_2 x_f, t - t_0 - x_E - x_f c_K - x_E - x c_R d x_f \right) \right)$$

where the coordinate x_f (unit: °E) is the longitude of the forcing $\tau_x(x_f, t)$, x_W (=130°E) and x_E (=280°E, i.e. 80°W) are the western and eastern boundaries, t is time in months, $c_{K/R}$ are the first mode Kelvin/Rossby wave speeds in °E per month (with $c_R = c_K/3$), τ_x^{3m} is the 3 months running mean of τ_x , and:

- if the field F_{eq} is the zonal current U_{eq} :

constant $C \sim 0.7 \text{ m s}^{-1} (\text{N/m}^2)^{-1} \text{ } ^\circ\text{E}^{-1}$; $t_0 \sim 0.5$ months; running mean $m_1 = m_2 = 2$ months and $d_1(x, x_f) = d_2(x, x_f) = \frac{1}{2} \frac{x_E - x}{x_E - x_W}$.

-if the field F_{eq} is SST_{eq} , the formula has a similar form¹, with:

¹ This approximated SST equation is mainly relevant in the western-central to eastern-central Pacific, not too close to the meridional boundaries, notably because of the crude

constant $C \sim 1.1^\circ\text{C}/(\text{N}/\text{m}^2)/^\circ\text{E}$; $t_0 \sim 1.5$ months; running mean $m_1 = 3$ months and $m_2 = 4$ months; $d_1(x, x_f) = \frac{x-x_f}{\frac{1}{2}(x_E-x_f)}$ and $d_2(x, x_f) = \frac{x_f-x}{x_f-x_W}$.

-if the field F_{eq} is SSH, the pattern is a priori more complex (cf. Fig. 3), but if the effect of the reflexion to the east is neglected, we can keep an almost similar form (not shown).

This formula could appear complex at first sight, but can be actually simply interpreted. The two integrals on the right hand side of the equation are of similar form, and physically represent the two cases $x_f < x$ and $x_f > x$. And within each integral, the two terms represent the fast positive response of the ocean to the westerly pulse followed by the delayed negative feedback (cf. Fig. 3).

We emphasize that these formulae are *very* crude. Their main purpose is to help to physically understand the equatorial oceanic response to various forcing cases.

References

Annamalai H, Xie SP, McCreary JP, Murtugudde R (2005) Impact of Indian Ocean sea surface temperature on developing El Niño. *J Clim* 18:302–319

Annamalai H, Kida S, Hafner J (2010) Potential impact of the tropical Indian Ocean–Indonesian Seas on El Niño characteristics. *J Clim* 23:3933–3952

Barnston, A. G., M. K. Tippett, M. L. L’Heureux, S. Li, and D. G. DeWitt (2011), Skill of Real-Time Seasonal ENSO Model Predictions during 2002–11: Is Our Capability Increasing?, *Bull. Am. Meteorol. Soc.*, 93(5), 631–651, doi:10.1175/BAMS-D-11-00111.1

Battisti DS, Hirst AC (1989) Interannual variability in the tropical atmosphere-ocean model: influence of the basic state, ocean geometry and nonlinearity. *J Atmos Sci* 45:1687–1712

Bollasina MA, Ming Y (2013) The general circulation model precipitation bias over the southwestern equatorial Indian Ocean and its implications for simulating the South Asian monsoon. *Clim Dyn.* doi:10.1007/s00382-012-1347-7.

Boulanger, J.-P., and C. Menkes (2001), The TRIDENT Pacific model: II. The thermodynamical model and the role of long equatorial wave reflection during the 1993–1998 TOPEX/POSEIDON period, *Clim. Dyn.*, 17, 175–186.

Boulanger, J.-P., C. Menkes, and M. Lengaigne (2004), Role of high-and low-frequency winds and wave reflection in the onset, growth and termination of the 1997–1998 El Niño, *Clim. Dyn.*, 22(2-3), 267–280.

Burgers G. and G.J. van Oldenborgh (2003) On the Impact of Local Feedbacks in the Central Pacific on the ENSO Cycle. *J. Clim.* 16, 2356.

Burgers G (2005) The simplest ENSO recharge oscillator. *Geophys Res Lett* 32(13):L13706.

parameterizations of the surface flux in the west and of the vertical term in the extreme-east Pacific

doi:10.1029/2005GL022951

Cane, M. A., and E. Sarachik (1979), Forced baroclinic ocean motion: III. The linear equatorial basin case, *J. Mar. Res.*, 39, 355–398.

Chen D, Zebiak SE, Busalacchi AJ, Cane MA (1995) An improved procedure for El Niño forecasting. *Science* 269: 1699–1702

Clarke, A.J. (1991), On the reflection and transmission of low-frequency energy at the irregular western Pacific Ocean boundary, *J. Geophys. Res.*, 96 , 3289-3305.

Clarke, A. J. (2014), El Niño Physics and El Niño Predictability, *Annu. Rev. Mar. Sci.*, 6(1), 311 79–99, doi:10.1146/annurev-marine-010213-135026.

Clarke AJ, Van Gorder S (2003) Improving El Niño prediction using a space-time integration of Indo-Pacific winds and equatorial Pacific upper ocean heat content. *Geophys Res Lett* 30(7):1399. doi:10.1029/2002GL016673

Dayan H, Vialard J, Izumo T, Lengaigne M (2014a) Does sea surface temperature outside the tropical Pacific contribute to enhanced ENSO predictability? *Clim Dyn.* doi:10.1007/s00382-013-1946-y

Dayan, H., T. Izumo, J. Vialard, M. Lengaigne and S. Masson (2014b): Do regions outside the tropical Pacific influence ENSO through atmospheric teleconnections?, *Climate Dynamics*, in revision.

Dee, and Coauthors (2011) The ERA-Interim reanalysis: configuration and performance of the data assimilation system. *Q. J. R. Meteorol. Soc.*, 137: 553–597. doi: 10.1002/qj.828.

Du Y, Xie S-P, Huang G, Hu K (2009) Role of air–sea interaction in the long persistence of El Niño-induced North Indian Ocean Warming*. *J Clim* 22:2023–2038

Florenchie P. and C. Perigaud (2002) Role of the western Pacific Ocean boundary conditions during 1980–1998 in the El Niño–Southern Oscillation events simulated by a coupled ocean–atmosphere model. *J. Geophys. Res.*, 107, C1, 3002, 10.1029/2000JC000615

Frauen C, Dommenges D (2012) Influences of the tropical Indian and Atlantic Oceans on the predictability of ENSO. *Geophys Res Lett* 39:L02706. doi:10.1029/2011GL050520

Gill AE (1980) Some simple solutions for heat-induced tropical circulation. *Q J R Meteorol Soc* 106:447–462.

Han, W., 2005: Origins and dynamics of the 90-day and 30–60-day variations in the equatorial Indian Ocean. *J. Phys. Oceanogr.*, 35, 708–728.

Hendon H. (2003) Indonesian Rainfall Variability: Impacts of ENSO and Local Air–Sea Interaction. *J. Clim.* 16, 1775.

Hendon, H. H., E.-P. Lim, J. Arblaster and D. L. T. Anderson (2013) Causes and predictability of the record wet east Australian spring 2010. *Clim. Dyn.*, DOI 10.1007/s00382-013-1700-5

Izumo T, de Boyer Montegut C, Luo J-J, Behera SK, Masson S, Yamagata T (2008) The role of the western Arabian Sea upwelling in Indian monsoon rainfall variability. *J Clim* 21:5603–5623

Izumo T, Vialard J, Lengaigne M, de Boyer Montegut C, Behera SK, Luo JJ, Cravatte S, Masson S, Yamagata T (2010) Influence of the state of the Indian Ocean Dipole on the following year's El Niño. *Nat Geosci* 3:168–172. doi:10.1038/ngeo760

- Izumo T, Lengaigne M, Vialard J, Luo J-J, Yamagata T, Madec G (2014) Influence of Indian Ocean Dipole and Pacific recharge on following year's El Niño: interdecadal robustness. *Clim Dyn* 42(1-2):291-310
- Jansen MF, Dommenges D, Keenlyside N (2009) Tropical atmosphere-ocean interactions in a conceptual framework. *J Clim* 22:550-567
- Jourdain N, M. Lengaigne, J. Vialard, T. Izumo and A. SenGupta (2014) Further insights on the influence of the Indian Ocean Dipole on following year's El Niño-Southern Oscillation in observations and CMIP5 models, submitted to *J. Clim.*
- Klein SA, Soden BJ, Lau N-C (1999) Remote sea surface temperature variations during ENSO: evidence for a tropical atmospheric bridge. *J Clim* 12:917-932
- Kug J-S, Kang I-S (2006) Interactive feedback between the Indian Ocean and ENSO. *J Clim* 19:1784-1801
- Lagerloef, G.S.E., G. Mitchum, R. Lukas and P. Niiler (1999) Tropical Pacific near-surface currents estimated from altimeter, wind and drifter data. *J. Geophys. Res.*, 104, 23,313-23,326.
- Lengaigne M, Boulanger J-P, Menkes C, Delecluse P, Slingo J (2004) Westerly wind events in the tropical Pacific and their influence on the coupled ocean-atmosphere system: a review. In: *Earth climate: the ocean-atmosphere interaction*, Geophys. Monogr. Ser., 147. AGU, Washington, DC, pp 49-69
- Lengaigne, M., J.-P. Boulanger, C. Menkes and H. Spencer (2006) Influence of the Seasonal Cycle on the Termination of El Niño Events in a Coupled General Circulation Model, *J. Clim.*, 19, 9, 1850-1868, doi:10.1175/JCLI3706.1
- Lloyd J, Guilyardi E, Weller H (2010) The role of atmosphere feedbacks during ENSO in the CMIP3 models. Part II: using AMIP runs to understand the heat flux feedback mechanisms. *Clim Dyn* 37:1271-1292.
- Luo J-J, Zhang R, Behera S, Masumoto Y, Jin F-F, Lukas R, Yamagata T (2010) Interaction between El Niño and extreme Indian Ocean Dipole. *J Clim* 23:726-742.
- McCreary, J.P. (1980) Modelling wind-driven ocean circulation. *JIMAR* 80-0029, *HIG* 80-3, Univ. of Hawaii, Honolulu, 64 pp.
- McCreary Jr., J.P. (1981) A linear stratified ocean model of the Equatorial Undercurrent. *Philosophical Transactions of the Royal Society of London* 298A, 603-635.
- McCreary, J.P., T. Miyama, R. Furue, T. Jensen, H.-W. Kang, B. Bang, and T. Qu (2007) Interactions between the Indonesian Throughflow and circulations in the Indian and Pacific Oceans. *Progr. in Oceanography*, 75 (1), 70-114.
- McGregor, S., N. J. Holbrook, and S. B. Power (2009) The response of a stochastically forced ENSO model to observed off-equatorial wind-stress forcing. *J. Climate*, 22, 2512-2525.
- McPhaden, M. J., A. J. Busalacchi, R. Cheney, J. R. Donguy, K. S. Gage, D. Halpern, M. Ji, P. Julian, G. Meyers, G. T. Mitchum, P. P. Niiler, J. Picaut, R. W. Reynolds, N. Smith, K. Takeuchi (1998) The Tropical Ocean-Global Atmosphere (TOGA) observing system: A decade of progress. *J. Geophys. Res.*, 103, 14,169-14,240.
- McPhaden, M. J., S. E. Zebiak, and M. H. Glantz (2006a), ENSO as an Integrating Concept in Earth Science, *Science*, 314(5806), 1740-1745, doi:10.1126/science.1132588.

- Meehl GA, Arblaster JM, Loschnigg J (2003) Coupled ocean- atmosphere dynamical processes in the tropical Indian and Pacific Ocean regions and the TBO. *J Clim* 16:2138–2158
- Meinen CS, McPhaden MJ (2000) Observations of warm water volume changes in the equatorial Pacific and their relationship to El Niño and La Nina. *J Clim* 13:3551–3559
- Moore, D. W., and J.P. McCreary, (1990) Excitation of intermediate frequency equatorial waves at a western ocean boundary: With application to observations from the Indian Ocean, *J. Geophys.Res.*, 95, 5192- 5231.
- Murtugudde R, McCreary JP, Busalacchi AJ (2000) Oceanic processes associated with anomalous events in the Indian Ocean with relevance to 1997–1998. *J Geophys Res* 105:3295–3306
- Neelin, J. D., The slow sea surface temperature mode and the fastwave limit: analytic theory for tropical interannual oscillations and experiments in a hybrid coupled models, *J. Atmos. Sci.*, 48, 584–606, 1991.
- Ohba M, Ueda H (2005) Basin-wide warming in the equatorial Indian Ocean associated with El Niño. doi:10.2151/sola
- Ohba M, Ueda H (2007) An impact of SST anomalies in the Indian Ocean in acceleration of the El Niño to La Nina transition. *J Meteorol Soc Jpn* 85:335–348
- Ohba M, Ueda H (2009a) Role of nonlinear atmospheric response to SST on the asymmetric transition process of ENSO. *J Clim*. 22:177–192
- Ohba M, Ueda H (2009b) Seasonally different response of the Indian Ocean to the remote forcing of El Niño: linking the dynamics and thermodynamics. *SOLA* 5:176–179. doi:10.2151/sola.2009-045.
- Ohba M., D. Nohara, and H. Ueda (2010) Simulation of asymmetric ENSO transition in WCRP CMIP3 multimodel experiments. *J. Climate*, 23, 6051–6067.
- Ohba M, Watanabe M (2012) Role of the Indo-Pacific interbasin coupling in predicting asymmetric ENSO transition and duration. *J Clim* 25(9):3321–3335.
- Ohba M. (2013) Important factors for long-term change in ENSO transitivity. *J. Inter.Clim.* 33 :1495-1509.
- Oppenheim, Alan V., Willsky, Alan S., and Young, Ian T. (1983) *Signals and Systems*, p. 256 (Englewood Cliffs, New Jersey: Prentice-Hall, Inc.) ISBN 0-13-809731-3.
- Palmer T.N. and Mansfield D.A. (1984) Response of two atmospheric general circulation models to sea-surface temperature anomalies in the tropical East and West Pacific. *Nature* **310**(5977): 483.
- Perigaud, C., and B. Dewitte (1996) El Niño–La Nina events simulated with Cane and Zebiak’s model and observed with satellite or in situ data. Part I: Model data comparison. *J. Climate*, **9**, 66–84.
- Picaut J., Ioualalen M., Menkes C., Delcroix T. and M.J. McPhaden (1996) Mechanism of the zonal displacements of the Pacific warm pool: implications for ENSO, *Science*, **274**, 1486-1489.
- Picaut J, Masia F, du Penhoat Y (1997) An advective-reflective conceptual model for the oscillatory nature of the ENSO. *Science* 277:663–666

- Prodhomme C., P. Terray, S. Masson, T. Izumo, T. Tozuka, and T. Yamagata (2013), Impacts of Indian Ocean SST biases on the Indian Monsoon as simulated in a global coupled model, *Climate Dynamics*, 42, 271-290
- Rayner NA, Parker DE, Horton EB, Folland CK, Alexander LV, Rowell DP, Kent EC, Kaplan A (2003) Global analyses of sea surface temperature, sea ice, and night marine air temperature since the late nineteenth century. *J Geophys Res* 108(D14):4407. doi:10.1029/2002JD002670
- Reverdin G, Cadet D, Gutzler D (1986) Interannual displacements of convection and surface circulation over the equatorial Indian Ocean. *Q J R Meteorol Soc* 112:43–46
- Reynolds RW, Rayner NA, Smith TM, Stokes DC, Wang W (2002) An improved in situ and satellite SST analysis for climate. *J Clim* 15:1609–1625
- Roeckner E. and Coauthors (2003) The atmospheric general circulation model ECHAM5. Part I: model description. Max Planck Institute for Meteorology Rep. 349, 127 pp
- Saji NH, Goswami BN, Viayachandran PN, Yamagata T (1999) A dipole mode in the tropical Indian Ocean. *Nature* 401:360–363
- Santoso A, England MH, Cai W (2012) Impact of Indo-Pacific feedback interactions on ENSO dynamics diagnosed using ensemble climate simulations. *J Clim* 25:7743–7763. <http://dx.doi.org/10.1175/JCLI-D-11-00287.1>
- Schopf PS, Suarez MJ (1988) Vacillations in a coupled ocean-atmosphere model. *J Atmos Sci* 45:549–566
- Schott, F. A., S.-P. Xie, and J. P. McCreary Jr. (2009), Indian Ocean circulation and climate variability, *Rev. Geophys.*, 47, RG1002, doi:10.1029/2007RG000245.
- Schwarzkopf, F. U., and C. W. Böning (2011), Contribution of Pacific wind stress to multidecadal variations in upper ocean heat content and sea level in the tropical south Indian Ocean, *Geophys. Res. Lett.*, 38, L12602, doi:10.1029/2011GL047651
- Shinoda, T., H.H. Hendon, M.A. Alexander (2004a) Surface and subsurface dipole variability in the Indian Ocean and its relation to ENSO . *Deep Sea Res.*, I, 51, 619-635.
- Shinoda, T., M.A. Alexander, H.H. Hendon (2004b) Remote response of the Indian Ocean to interannual SST variations in the tropical Pacific . *J. Climate*, 17, 362-372.
- Shu L. and A.J. Clarke (2002) Using an Ocean Model to Examine ENSO Dynamics. *J. Phys. Oceanogr.* 32, 903.
- Spencer H (2004) Role of the atmosphere in seasonal phase locking of El Niño. *Geophys Res Lett* 31:L24104. doi:10.1029/2004GL021619
- Suresh, I., J. Vialard, M. Lengaigne, W. Han, J. McCreary, F. Durand, and P. M. Muraleedharan (2013), Origins of wind-driven intraseasonal sea level variations in the North Indian Ocean coastal waveguide, *Geophys. Res. Lett.*, 40, doi:10.1002/2013GL058312.
- Tiedtke M (1989) A comprehensive mass flux scheme for cumulus parameterization in large-scale models. *Mon Weather Rev* 117(8):1779–1800
- Trenberth KE, Branstator GW, Karoly D, Kumar A, Lau N-C, Ropelewski C (1998) Progress during TOGA in understanding and modeling global teleconnections associated with tropical sea surface temperatures. *J Geophys Res* 103(C7):14291–14324. doi:10.1029/97JC01444

- Vialard J, Menkes C, Boulanger J-P, Delecluse P, Guilyardi E, McPhaden M (2001) A model study of the oceanic mechanisms affecting the equatorial SST during the 1997–98 El Niño. *J Phys Oceanogr* 31:1649–1675
- Watanabe M, Jin F-F (2002) Role of Indian Ocean warming in the development of the Philippine Sea anticyclone during El Niño. *Geophys Res Lett* 29. doi:10.1029/2001GL014318
- Webster PJ, Moore AM, Loschnigg JP, Leben RR (1999) Coupled oceanic–atmospheric dynamics in the Indian Ocean during 1997– 98. *Nature* 401:356–360
- Wentz FJ, Gentemann C, Smith D, Chelton D (2000) Satellite measurements of sea-surface temperature through clouds. *Science* 288:847–850
- Xie S-P, Hu K, Hafner J et al (2009) Indian Ocean capacitor effect on Indo-Western Pacific climate during the summer following El Niño. *J Clim* 22:730–747
- Yamanaka G, Yasuda T, Fujii Y, Matsumoto S (2009) Rapid termination of the 2006 El Niño and its relation to the Indian Ocean. *Geophys Res Lett* 36:L07702. doi:10.1029/2009 GL037298
- Yuan, D. L., and Coauthors (2011) Forcing of the Indian Ocean dipole on the interannual variations of the tropical Pacific Ocean: Roles of the Indonesian throughflow. *J. Climate*, 15, 3597–3608.
- Zebiak SE, Cane MA (1987) A model El Niño-Southern Oscillation. *Mon Weather Rev* 115:2262–2278
- Zhao Y., Nigam S. (2015) The Indian Ocean Dipole: A Monopole in SST. *J.Climate*, 28, 3–19.

Table 1. Validation of the causal band-pass filtered τ_x method with observations. Correlation between observations and the estimate from the causal band-pass filtered $\tau_{x,cp}$ (in parenthesis if without delayed negative feedback, for comparison), for zonal current and thermocline depth/SSH (using same observations as in Fig. 2). The results are computed using physically-reasonable (in light of Fig. 3a,b) adjusted causal-filtered parameters given in the table for each location and field.

Correlation obs-causal filtered τ_x	0°N, 165°E	0°N, 170°W	0°N, 140°W
$U_{TAO}/U_{gAVISO}/U_{OSCAR}$	0.87/0.89/0.82 (0.84/0.83/0.73), using $\tau_x^{1m}(t) - \tau_x^{2m}(t-6)/2$	0.56/0.85/0.74 (0.20/0.74/0.54), using $\tau_x^{1m}(t) - 2/3 \tau_x^{2m}(t-6)$	0.62/0.79/0.47 (0.33/0.66/0.18), using $\tau_x^{1m}(t) - 2/3 \tau_x^{2m}(t-5)$
$z20_{TAO}/SSH_{AVISO}$	0.86/0.49 (-0.62/-0.01), using $\tau_x^{1m}(t)/3 - \tau_x^{6m}(t-4)$	0.56/0.82 (0.11/0.75), using $\tau_x^{1m}(t) - 2/3 \tau_x^{6m}(t-6)$	0.90/0.90 (0.69/0.83), using $\tau_x^{3m}(t-1) - 2/3 \tau_x^{8m}(t-6)$

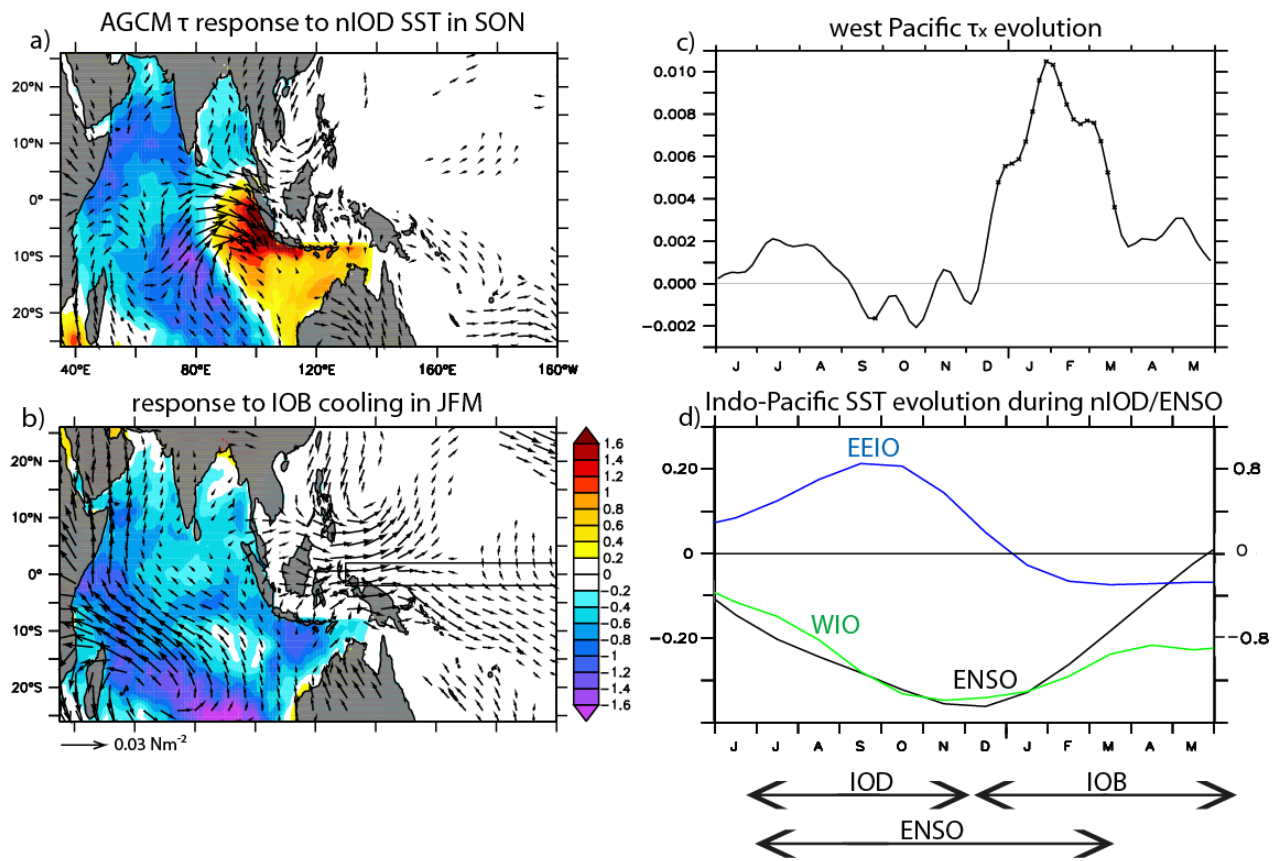


Fig. 1. a) Wind stress (black vectors, in N.m^{-2}) response of the AGCM to a « negative » IOD (and IOB) SST forcing (colour shading, in $^{\circ}\text{C}$) in Sep-Nov (cf. section 2 for details); b) as in a) for following IOB cooling in Jan-March. c) Temporal evolution of zonal wind stress $\tau_{x,wp}$ averaged in the western Pacific (130°E - 160°W , 2°S - 2°N ; region shown as a box in Fig. 1b) in this AGCM experiment, with crosses indicating zonal wind stress significant at the 90% level. The « negative » IOD case shown here is inferred from: $(\text{nIOD}-\text{pIOD})/2$ (for nIOD/pIOD events of $2\sigma_{\text{IOD}}$, cf. text). d) Temporal evolution of SST indices in Niño3.4 (black), Eastern Equatorial Indian Ocean (EEIO, i.e. DMI eastern pole; blue), Western IO (WIO, i.e. DMI western pole; green) during nIOD (and often concurrent ENSO/IOB negative phase), inferred from the regression on $-\text{DMI}$ in SON using OISSTv2 observed SST (the left scale is for WIO, the right one, 4 times higher, is for EEIO and ENSO; see Schott et al. 2009, their Fig. 12, for an equivalent figure, but based on ENSO). The EEIO warming tends to counteract WIO cooling, and thus IOB development and related $\tau_{x,wp}$. By convention all figures show the case of a negative IOD (+IOB cooling) of $2\sigma_{\text{IOD}}$ (*vice versa* for a positive IOD followed by IOB warming).

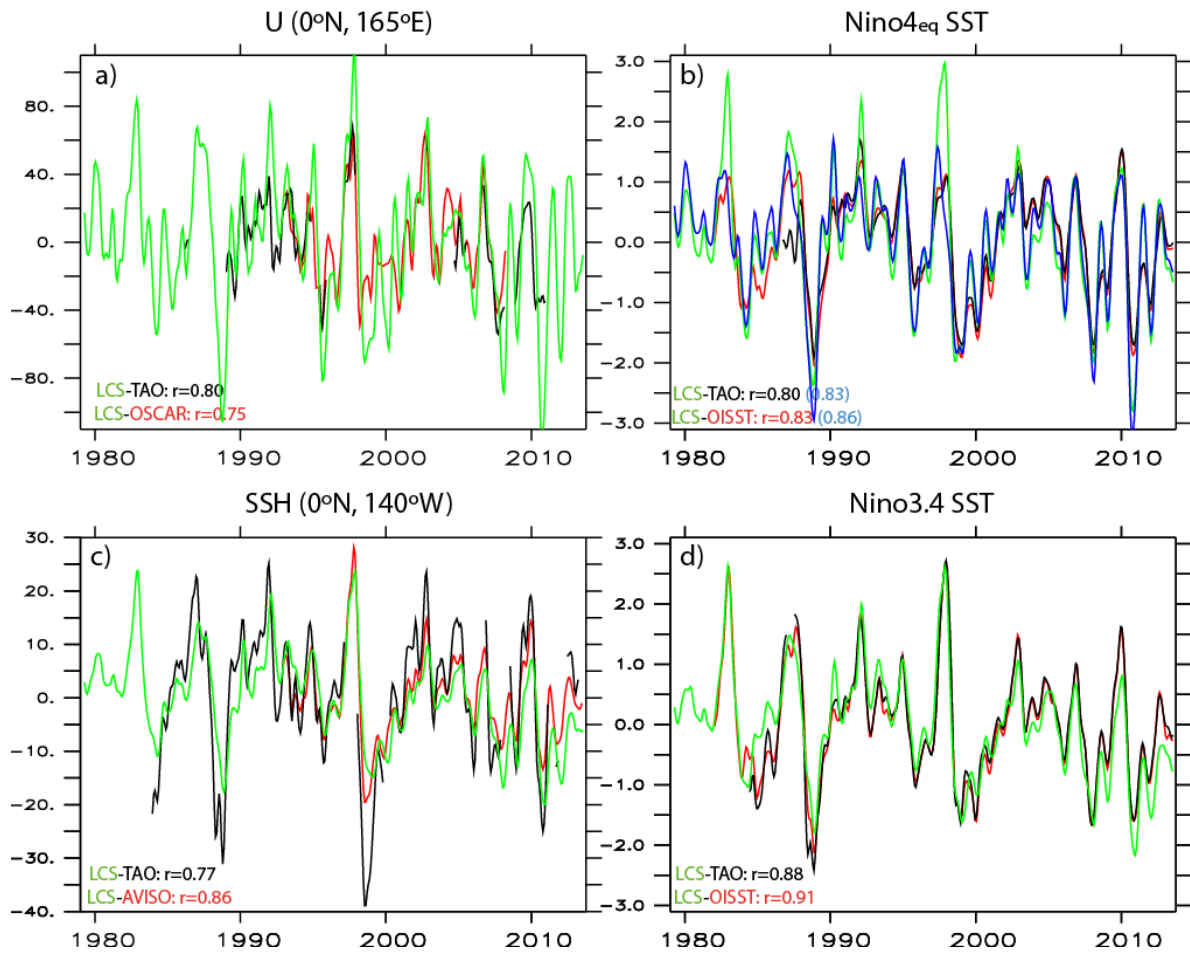


Fig. 2. Validation of the LCS ocean model (green) with *in situ* TAO data (black) and satellites-related products (red), for the central-west (upper panels) and central-east (lower panels) Pacific. a) zonal current U at 0°, 165°E (cm/s, 0-20m, red is for OSCAR product). c) SSH at 0°, 140°W (cm, red is for AVISO, black is for TAO thermocline depth z_{20} (m/1.5)). b) SST (°C) in Niño_{4eq} region (blue curve if interannually varying SST gradient used, see text). d) SST in Niño_{3.4}. The correlations r are between the LCS and the various observational datasets.

LCS equatorial response to a Niño-like westerly pulse

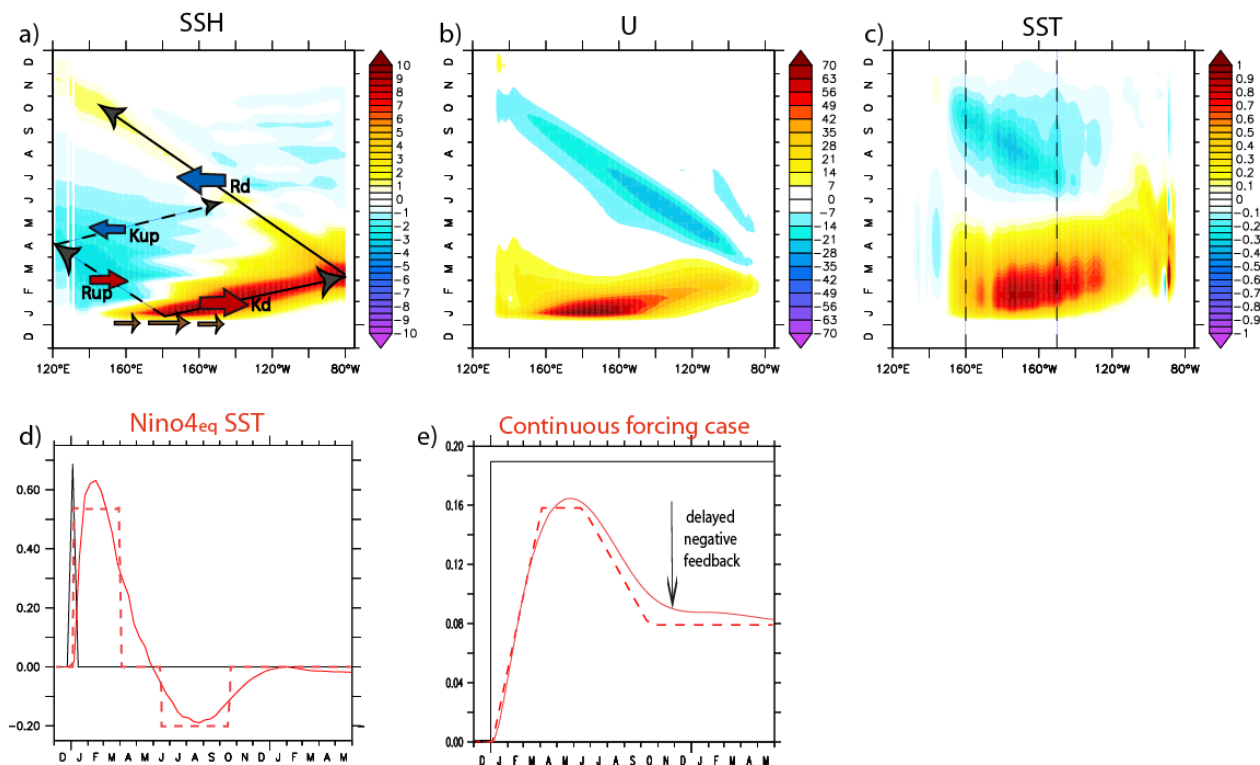


Fig. 3. Equatorial impulse response to an « ENSO-like » $\tau_{x,cp}$ westerly windstress pulse in the central-west Pacific for a) SSH (cm), b) U (cm.s⁻¹), c) SST (°C) and d) Niño4_{eq} SST (red line). In **d**, the $\tau_{x,cp}$ pulse (N.m⁻²×10) averaged over 2°N-2°S, 140°E-140°W (region centred on the idealised patch) is shown in black, and the « causal filter » approximation (red dashes) as a difference of two running-box filters (3 months and 4 months) lagged by 6 months for $\tau_{x,cp}$ (cf. equation 3). **e**) Time integral of the impulse response shown in **d**, i.e. the oceanic response (red) to a continuous wind forcing $\tau_{x,cp}$ starting in January (black, same amplitude A as the pulse), and of its approximation (red dashes). In **a**, the brown arrows indicate the wind stress pulse. The Kelvin (K) and Rossby (R) wave responses are indicated by thin black arrows (continuous line for downwelling (d) and dashed for upwelling (up) waves). The resulting zonal current anomalies are indicated by red (eastward) and blue (westward) arrows. In **c**, the vertical dashed lines show the Niño4_{eq} longitude range.

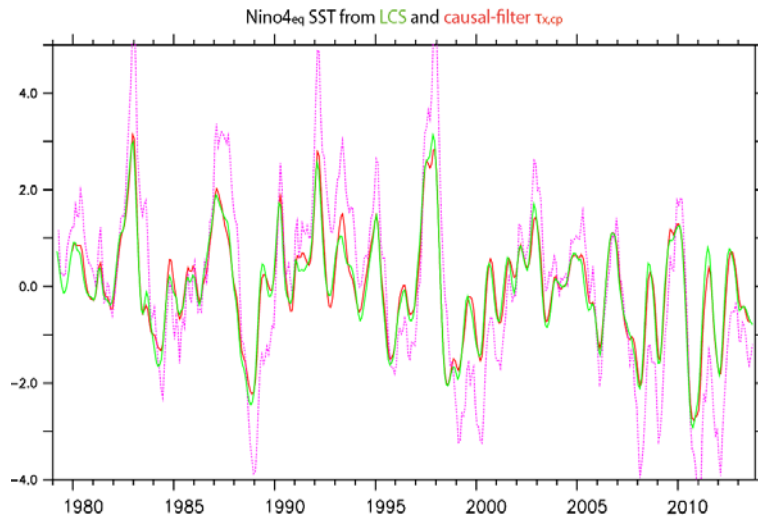


Fig. 4. Validation of the convolution/causal-filter approximation for Niño_{4eq} SST inferred from the impulse response to central Pacific westerlies. Exact LCS Niño_{4eq} SST (green) and causal-filtered $\tau_{x,cp}$ (red, using equation (4) with a 1.34 correction factor; $r=0.98$). Purple dots show the estimate if the delayed negative feedback (i.e. the 2nd peak in Fig. 3d and equation (4)) is not taken into account ($r=0.84$; explained variance then only of 71%, instead of 96% for the red curve).

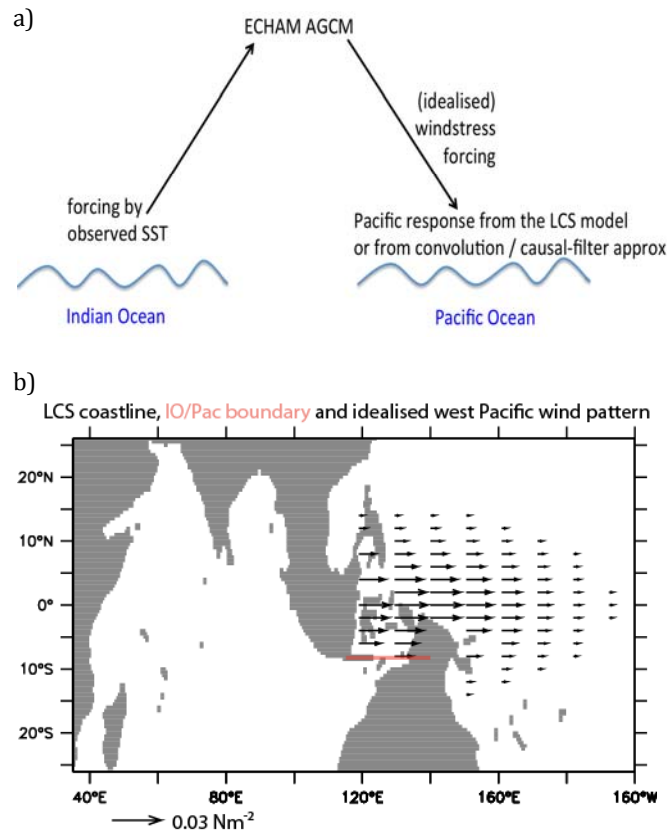


Fig. 5. a) Schematics of the combined AGCM-LCS experimental setup. b) Gaussian pattern of τ_x in the western Pacific forcing the idealised LCS experiments, mimicking the Jan-Mar response to the IOB, with the LCS « coastline » in grey (inferred from the 200m isobath) and the Indian Ocean/Pacific boundary at 8°S in red (a boundary used to define wind forcing associated to oceanic/atmospheric bridges).

LCS equatorial response to an IOB-like westerly pulse

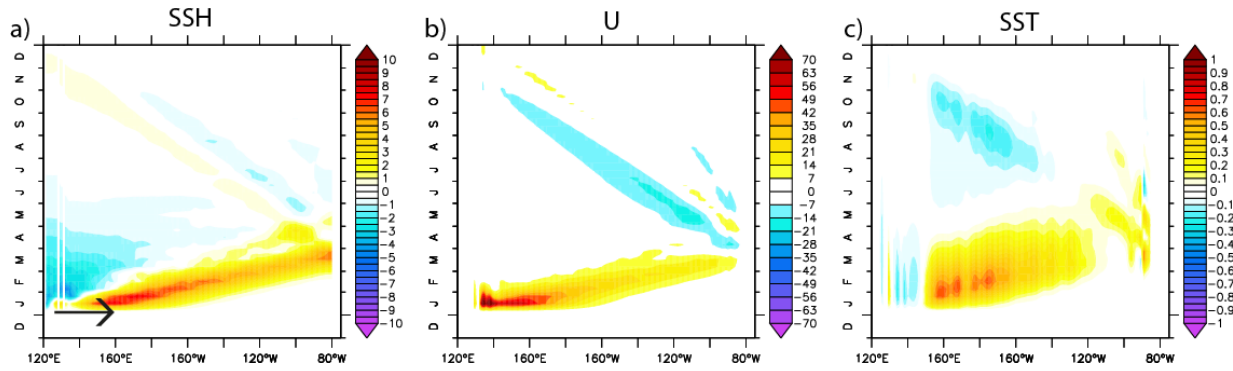


Fig. 6. Same as Fig. 3a,b,c, here for the western Pacific westerly pulse forcing (the IOB-like wind pattern shown in Fig. 5c).

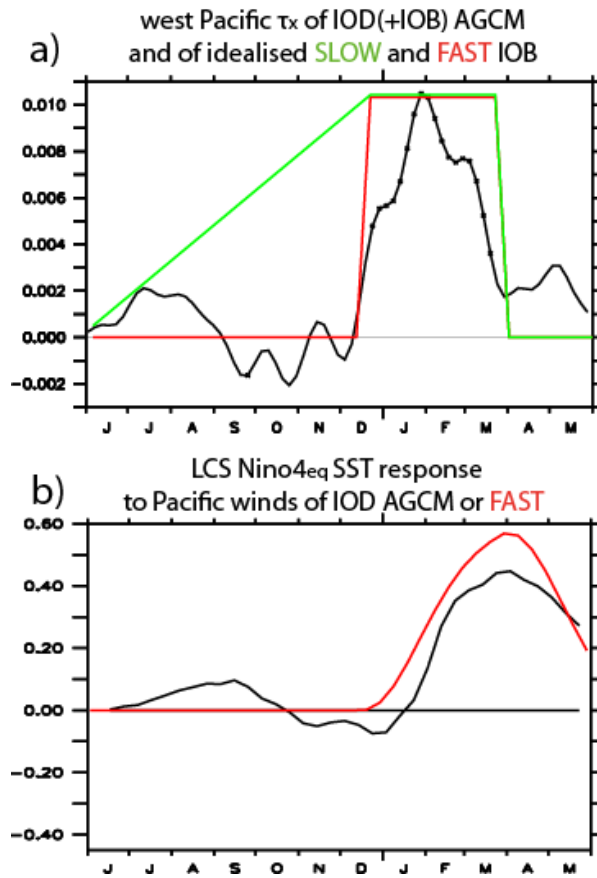


Fig. 7. a) Temporal evolution of the zonal windstress $\tau_{x,wp}$ in the western Pacific (130°E-160°W, 2°S-2°N), in black for the IOD(+IOB)-forced AGCM experiment as in Fig. 1c. The green and red lines represent the idealised forcing for the « SLOW » IOB forcing (IOB only) and « FAST » IOB appearance (IOD+IOB) cases. b) LCS Niño_{4eq} SST response to the Pacific windstress of this IOD(+IOB)-forced AGCM experiment (black) or of the idealised « FAST » IOB case (red).

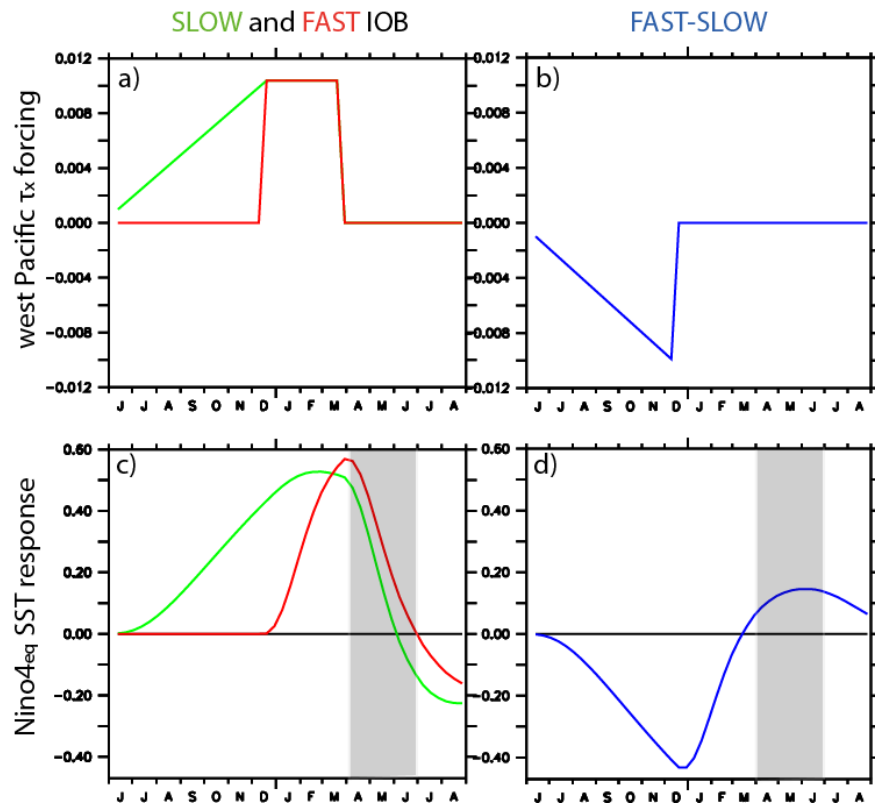


Fig. 8. Comparison of SLOW (green) and FAST (red) idealised experiments, to better understand IOB and IOD relative influences. The difference FAST-SLOW (blue) is shown in the right panels. Upper: western Pacific $\tau_{x,wp}$ forcing. Lower: Niño_{4eq} SST response. The shaded zone represents the April-June averaging period used in Fig. 9.

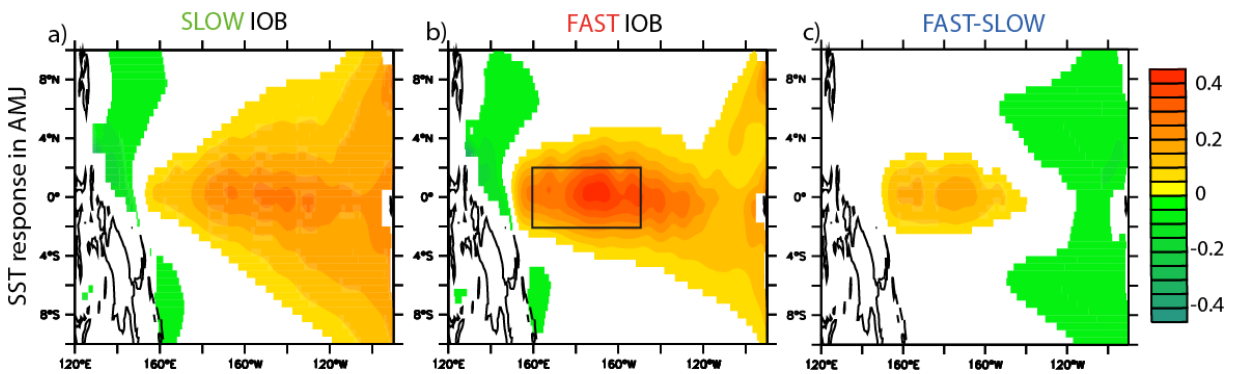


Fig. 9. SST response in April-June of a) SLOW and b) FAST idealised experiments. c) Difference FAST-SLOW. The black box in **b** shows the Niño_{4eq} region.

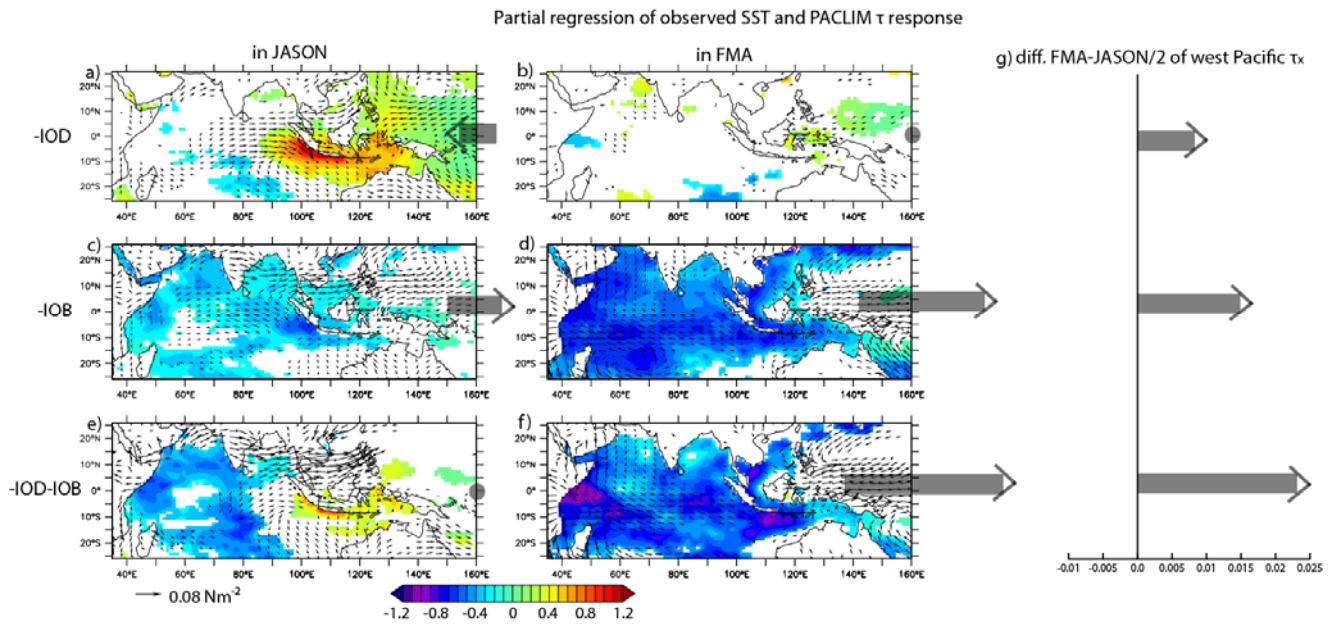


Fig. 10. Respective influences of IOD and IOB on west Pacific $\tau_{x,wp}$ evolution from JASON (July-November) to FMA (February-April). The left (JASON) and central (FMA) columns display the observed SST ($^{\circ}\text{C}$, color shading) and the windstress response of the PACLIM AGCM experiment (black arrows, Nm^{-2}) partially regressed on $-\text{IOD}$ (1st line) or $-\text{IOB}$ (2nd line), with their sum representing $-\text{IOD}-\text{IOB}$ case (3rd line; partial correlation method; see text for details). The thick grey arrows show the corresponding western Pacific wind stress response (when significant at the 90% level), their length being proportional to the windstress amplitude in Nm^{-2} . The last column shows the difference between the FMA and one half of the JASON wind stress anomalies, linked to the late spring central Pacific SST response through equation (6) in the manuscript. A “pure nIOD”, with its large eastern pole and weaker western pole, forces significant $\tau_{x,wp}$ easterlies in JASON but not in FMA, leading to a significant FMA-JASON/2 difference in $\tau_{x,wp}$. A “pure nIOB” forces significant $\tau_{x,wp}$ westerlies during both seasons, but are stronger in FMA, leading to a significant FMA-JASON/2 $\tau_{x,wp}$. When an IOB occurs with an IOD, the IOD tends to cancel out IOB-forced $\tau_{x,wp}$ westerlies in JASON, but not in FMA, leading to a larger FMA-JASON/2 $\tau_{x,wp}$ than in the pure IOB case.

Partial reg. on -IOD or -IOB, and sum

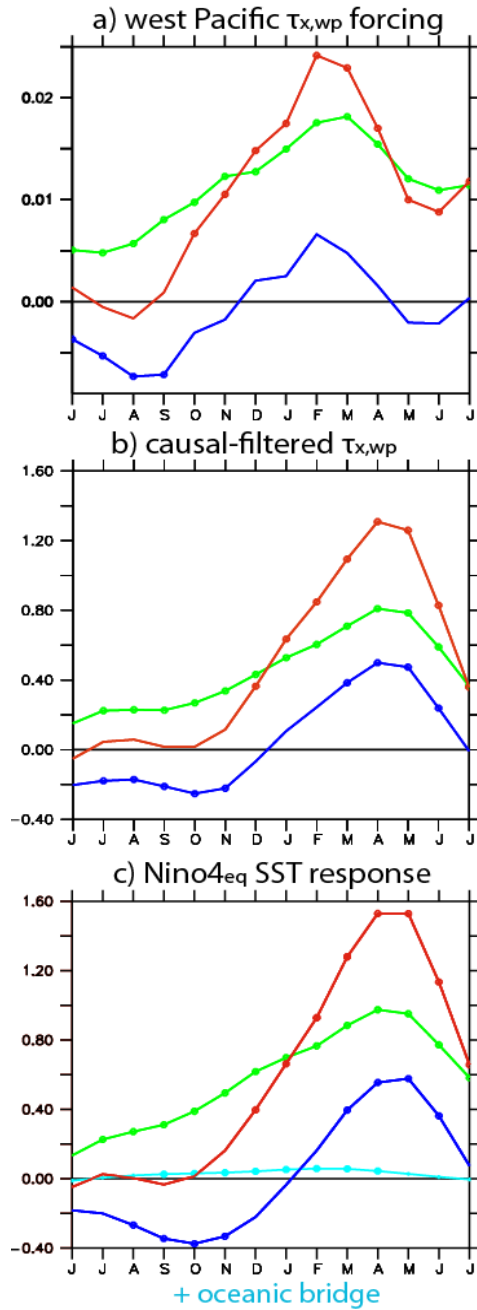


Fig. 11. IOD and IOB respective influences in PACLIM set of experiments on **a)** AGCM west Pacific $\tau_{x,wp}$ ($\text{N}\cdot\text{m}^{-2}/2\sigma_{\text{IODorIOB}}$), **b)** causal-filtered $\tau_{x,wp}$, cf. equation (5) and **c)** LCS Niño4_{eq} SST (lower panels) ($^{\circ}\text{C}/2\sigma_{\text{IODorIOB}}$), inferred from the partial regression on -IOD without IOB influence (dark blue) and on -IOB without IOD influence (green; similar method as in Fig. 10). Their sum, i.e. “-IOD-IOB”, is shown in red. In **c)**, the weak oceanic bridge effect of the IOD (cf. section 6.2) is shown in light blue, for comparison to the atmospheric bridge mainly discussed in the present study (e.g. the dark blue line in **c)**). A three months running mean is applied to all variables, to reduce intraseasonal noise. Dots on curves indicate signals significant at the 90% level.

Pure IOD, pure IOB, and IOD+IOB cases

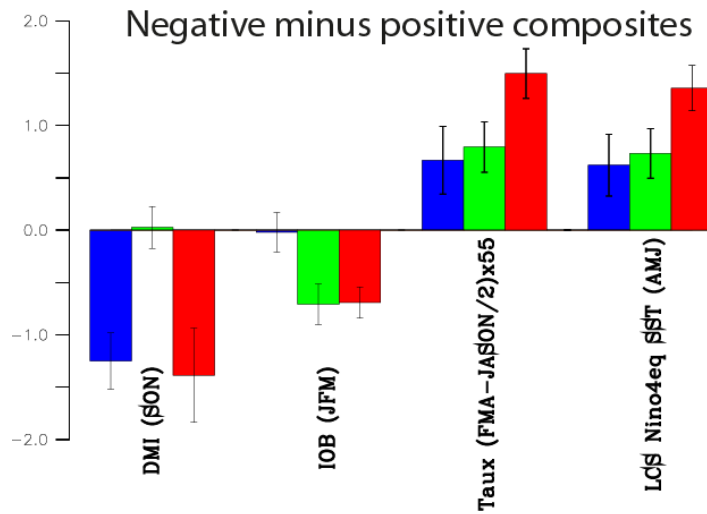


Fig. 12. Composites ($^{\circ}\text{C}$) of pure IOD (blue, 2 positive and 4 negative events), pure IOB (green, 4 pos. and 5 neg. events), IOD+IOB cases (red, 4 pos. and 2 neg. events; actual number of members: 7 per event), for DMI (SON) and IOB (JFM) indices (from the observed SST that forced PACLIM), and for the PACLIM AGCM $\tau_{x,wp}$ response $(\text{FMA-JASON}/2) \times 55$ (unit: $\text{N}/\text{m}^2 \times 55^{\circ}\text{C}/(\text{N}/\text{m}^2)$ equivalent to $^{\circ}\text{C}$, cf. equation (6)) and PACLIM LCS SST response in following spring (AMJ). We plot the difference between negative and positive composites (asymmetries between negative and positive events being not statistically significant; not shown). The composite difference shown here corresponds to pure nIOD/nIOB events of 2.4σ amplitude (σ_{IOD} and σ_{IOB} being of 0.52°C and 0.29°C respectively), hence close to the 2σ convention used in all other figures. For DMI and IOB forcing indices, the square root of the sum of the inter-event variances of DMI and IOB is shown as a thin bar. For the PACLIM ensemble responses, the 90% interval of confidence (evaluated from a Student t-test on the ensembles) is shown as a thick black bar.

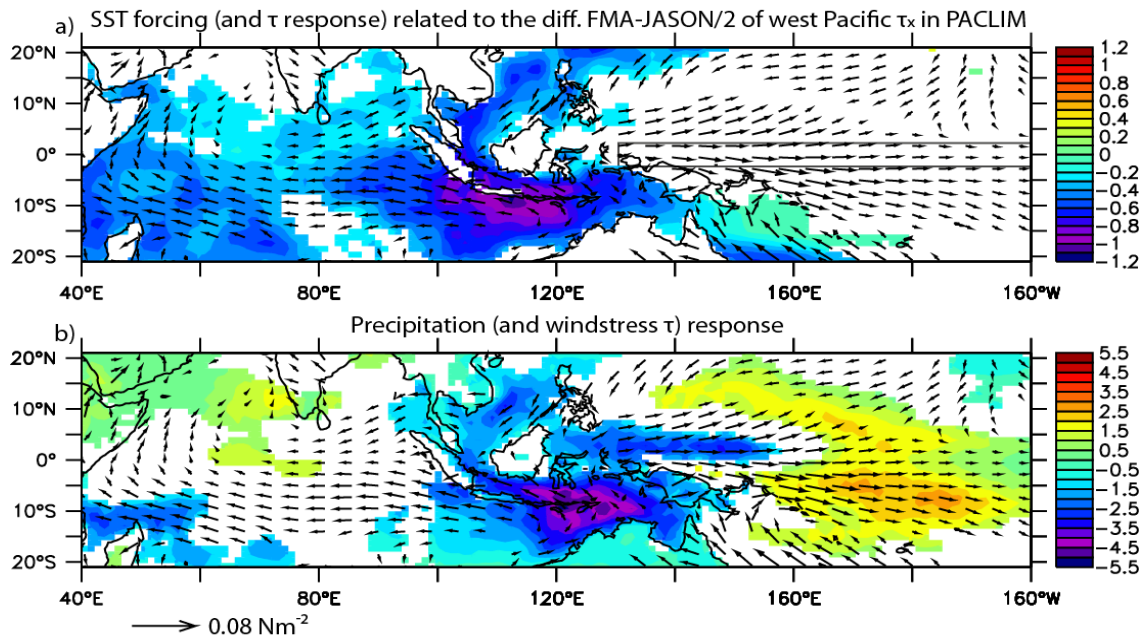


Fig. 13. Regression of observed SST (upper, that forces PACLIM AGCM experiment; °C) and precipitation (lower; mm.day⁻¹), plus windstress (vectors), on west Pacific $\tau_{x,wp}$ (averaged over the box region shown in **a**, as in Fig. 1a) of PACLIM experiment, for the difference FMA-JASON/2 (for both the regressed fields and $\tau_{x,wp}$). This figure shows that mainly the SST/precipitation seasonal change in the eastern Indian Ocean and maritime continent related to the transition from IOD to IOB is at the origin of this $\tau_{x,wp}$ difference, i.e. of a strong causal-filtered $\tau_{x,wp}$ anomaly.